



3D modelling of HCO^+ and its isotopologues in the low-mass proto-star IRAS16293–2422

D. Quenard, S. Bottinelli, E. Caux, Valentine Wakelam

► To cite this version:

D. Quenard, S. Bottinelli, E. Caux, Valentine Wakelam. 3D modelling of HCO^+ and its isotopologues in the low-mass proto-star IRAS16293–2422. *Monthly Notices of the Royal Astronomical Society*, 2018, 477 (4), pp.5312-5326. 10.1093/mnras/sty1004 . hal-01773955

HAL Id: hal-01773955

<https://hal.science/hal-01773955>

Submitted on 10 Feb 2023

HAL is a multi-disciplinary open access archive for the deposit and dissemination of scientific research documents, whether they are published or not. The documents may come from teaching and research institutions in France or abroad, or from public or private research centers.

L'archive ouverte pluridisciplinaire **HAL**, est destinée au dépôt et à la diffusion de documents scientifiques de niveau recherche, publiés ou non, émanant des établissements d'enseignement et de recherche français ou étrangers, des laboratoires publics ou privés.

3D modelling of HCO^+ and its isotopologues in the low-mass proto-star IRAS16293–2422

D. Quénard,^{1,2★} S. Bottinelli,¹ E. Caux¹ and V. Wakelam³

¹IRAP, Université de Toulouse, CNRS, UPS, CNES, F-31028 Toulouse, France

²School of Physics and Astronomy, Queen Mary University of London, Mile End Road, London E1 4NS, UK

³Laboratoire d'astrophysique de Bordeaux, Univ. Bordeaux, CNRS, B18N, allée Geoffroy Saint-Hilaire, F-33615 Pessac, France

Accepted 2018 April 13. Received 2018 March 14; in original form 2017 December 11

ABSTRACT

Ions and electrons play an important role in various stages of the star formation process. By following the magnetic field of their environment and interacting with neutral species, they slow down the gravitational collapse of the proto-star envelope. This process (known as ambipolar diffusion) depends on the ionization degree, which can be derived from the HCO^+ abundance. We present a study of HCO^+ and its isotopologues (H^{13}CO^+ , HC^{18}O^+ , DCO^+ , and D^{13}CO^+) in the low-mass proto-star IRAS16293–2422. The structure of this object is complex, and the HCO^+ emission arises from the contribution of a young NW-SE outflow, the proto-stellar envelope, and the foreground cloud. We aim at constraining the physical parameters of these structures using all the observed transitions. For the young NW-SE outflow, we derive $T_{\text{kin}} = 180\text{--}220\text{ K}$ and $n(\text{H}_2) = (4\text{--}7) \times 10^6\text{ cm}^{-3}$ with an HCO^+ abundance of $(3\text{--}5) \times 10^{-9}$. Following previous studies, we demonstrate that the presence of a cold ($T_{\text{kin}} \leq 30\text{ K}$) and low density [$n(\text{H}_2) \leq 1 \times 10^4\text{ cm}^{-3}$] foreground cloud is also necessary to reproduce the observed line profiles. We have used the gas-grain chemical code NAUTILUS to derive the HCO^+ abundance profile across the envelope and the external regions where $X(\text{HCO}^+) \gtrsim 1 \times 10^{-9}$ dominate the envelope emission. From this, we derive an ionization degree of $10^{-8.9} \lesssim x(\text{e}) \lesssim 10^{-7.9}$. The ambipolar diffusion time-scale is ~ 5 times the free-fall time-scale, indicating that the magnetic field starts to support the source against gravitational collapse and the magnetic field strength is estimated to be $6\text{--}46\mu\text{G}$.

Key words: astrochemistry – radiative transfer – methods: numerical – ISM: abundances – ISM: individual objects: IRAS16293–2422 – ISM: molecules.

1 INTRODUCTION

The ionization degree, defined as $x(\text{e}) = n(\text{e})/n(\text{H}_2)$ (with $n(\text{e})$ the electron density and $n(\text{H}_2)$ the H_2 density), plays an important role in regulating the star formation process (e.g. Mouschovias 1987; Shu, Adams & Lizano 1987). Indeed, through ambipolar diffusion, ions are separated from neutral species because of the ambient magnetic field. Due to collisions between ions and neutrals, the neutral matter, experiencing gravitational collapse, is slowed down from infalling into the central object. The time-scale for ambipolar diffusion (t_{AD}) depends on the ionization degree [$t_{\text{AD}}(\text{yr}) = 2.5 \times 10^{13} x(\text{e})$; Spitzer 1978; Shu et al. 1987]. If the ratio of time-scales between ambipolar diffusion and free-fall is close to one, the magnetic field is not playing any important role in preventing the collapse and it may lead to a situation where the object becomes gravitationally unstable. It

is therefore important to determine the ionization degree in order to understand the dynamics of a proto-stellar object.

HCO^+ has been proven to be a good tracer of the degree of ionization of a cloud because it indirectly probes the electron density when compared to other species (Caselli et al. 2002a,b,c). Moreover, around low-mass proto-stars, HCO^+ is expected to be abundant owing to the relative simplicity of its formation, making it easy to detect and to study.

IRAS16293–2422 (hereafter IRAS16293) is a typical solar-type Class 0 low-mass proto-star located at 147.3 pc (Ortiz-León et al. 2017) embedded in the LDN1689N cloud within the ρ Ophiuchus complex. This source is well studied due to its strong emission lines and its chemical richness (e.g. Caux et al. 2011; Jørgensen et al. 2011, 2016). Many physical and chemical processes have been tested using observations towards this object, making it a ‘template’ source in the past decades. The structure of this object is quite complex and several outflows have been detected and traced at multiple scales (Castets et al. 2001; Stark et al. 2004; Chandler

★ E-mail: d.quenard@qmul.ac.uk

et al. 2005; Yeh et al. 2008; Loinard et al. 2012; Girart et al. 2014). At small scales, it is composed of two distinct cores IRAS16293 A and IRAS16293 B separated by ~ 5 arcsec (Wootten 1989; Mundy et al. 1992). Little is known on the physical properties of these cores although more and more studies aim at understanding their structure (e.g. Chandler et al. 2005; Rao et al. 2009; Pineda et al. 2012; Jacobsen et al. 2018) and chemical content (e.g. Caux et al. 2011; Jørgensen et al. 2011, 2016; Persson et al. 2018). To derive an accurate abundance of HCO⁺ (and therefore the ionization degree), a complete description of the structure of the source is needed. Indeed, an estimation of the HCO⁺ abundance and some of its isotopologues in the envelope has already been obtained by van Dishoeck et al. (1995) and Schöier et al. (2002) but without taking into account the complex structure of the source.

The goal of this study is twofold: we aim at giving better constraints on the 3D physical structure of IRAS16293 and to derive an accurate value of the HCO⁺ abundance in the different environments of this source. To do so, we use the observed emission of HCO⁺ and its isotopologues (H¹³CO⁺, HC¹⁸O⁺, DCO⁺, and D¹³CO⁺), described in Section 2. We then compare these observations to 3D radiative transfer modellings, presented in Section 3. The 3D physical and chemical structure of the object is described in Section 4 and our method in Section 5. We derive constraints on the 3D physical structure of IRAS16293 in Section 6 together with discussions on the parameters used in this study. From our modelling of the HCO⁺ abundance, we are finally able to determine the ionization degree across the source. Concluding remarks are given in Section 7.

2 OBSERVATIONS

In this work, we are using data coming from two unbiased spectral surveys: (i) The IRAS16293 Millimetre and Sub-millimetre Spectral Survey, performed at the IRAM 30 m (80–265 GHz) and JCMT-15m (330–370 GHz) telescopes between 2004 January and 2006 August, and APEX-12m (265–330 GHz) telescope between 2011 June and 2012 August (TIMASSS; Caux et al. 2011) and (ii) the HIFI guaranteed time Key Program CHESS (Ceccarelli et al. 2010). The HIFI data presented in this article are part of a survey observed between 2010 March and 2011 April, providing full spectral coverage of bands 1a (480–560 GHz; obsid 1342191499), 1b (560–640 GHz; obsid 1342191559), 2a (640–720 GHz; obsid 1342214468), 2b (720–800 GHz; obsid 1342192332), 3a (800–880 GHz; obsid 1342214308), 3b (880–960 GHz; obsid 1342192330), 4a (960–1040 GHz; obsid 1342191619), 4b (1040–1120 GHz; obsid 1342191681), and 5a (1120–1200 GHz; obsid 1342191683). The HIFI Spectral Scan Double Beam Switch (DBS) observing mode with optimization of the continuum was used with the HIFI acousto-optic Wide Band Spectrometer (WBS), providing a spectral resolution of 1.1 MHz (~ 0.6 km s^{−1} at 500 GHz and ~ 0.3 km s^{−1} at 1 THz) over an instantaneous bandwidth of 4×1 GHz (Roelfsema et al. 2012).

For the TIMASSS survey, the observed coordinates were $\alpha_{2000} = 16^{\text{h}}32^{\text{m}}22^{\text{s}}.6$, $\delta_{2000} = -24^{\circ}28'33''$, while they were $\alpha_{2000} = 16^{\text{h}}32^{\text{m}}22^{\text{s}}.75$, $\delta_{2000} = 24^{\circ}28'34''.2$ for the HIFI observations. The difference in the aimed positions has been carefully taken into account in this work. For both surveys, the DBS reference positions were situated 3 arcmin apart from the source. Table 1 summarizes the observation parameters.

The data processing of the TIMASSS survey has been extensively described in Caux et al. (2011). The HIFI data have been processed using the standard HIFI pipeline up to frequency and in-

tensity calibrations (level 2) with the ESA-supported package HIPE 12 (Ott 2010). Using a standard routine developed within the HIFI ICC (Instrument Control Center), *flagTool*, spurs not automatically detected by the pipeline have been tagged and removed. Then, the HIPE tasks *fitHifiFringe* and *fitBaseline* were used to remove standing waves and to fit a low-order polynomial baseline to line-free channels. Finally, sideband deconvolution was performed with the dedicated HIPE task *doDeconvolution*.

The spectra observed in both horizontal and vertical polarizations were of similar quality, and averaged to lower the noise in the final spectrum, since polarization is not a concern for the presented analysis. The continuum values obtained from running *fitBaseline* are well fitted by polynomials of order 3 over the frequency range of the whole band. The single-side band continuum derived from the polynomial fit at the considered frequencies (Table 1) was added back to the continuum-free spectra. Intensities were then converted from antenna to main-beam temperature scale using a forward efficiency of 0.96 and the (frequency-dependent) beam-efficiency shown in Table 1. Peak intensities are reported in Table 1 together with the spectroscopic and observing parameters of the transitions used in this work.

3 RADIATIVE TRANSFER MODELLING

We have first tried to fit the detected lines using simpler radiative transfer models: Boltzmann diagrams, LTE modelling, and LVG calculations. None of these methods gave satisfactory results, thus, in order to derive the line profile of the studied molecular transitions and the continuum emission, we have used LIME, a 3D non-LTE radiative transfer code (Brinch & Hogerheijde 2010). To describe the input 3D physical model of IRAS16293 and set the different parameters of LIME we have used GASS (Generator of Astrophysical Sources Structures, Quéward, Bottinelli & Caux 2017a). GASS is a user-friendly interface that allows us to create, manipulate, and mix one or several different physical structures such as spherical sources, discs, and outflows. GASS is fully adapted to LIME and it produces output models that can be directly read by LIME. A complete description of the procedure that creates the different structures of the physical model is given in Quéward et al. (2017a).

Once output data cubes have been generated by LIME they have been post-processed using GASS. For single-dish observations, the treatment consists in convolving the cube with the beam size of the desired telescope and to plot the predicted spectrum in main beam temperature as a function of the velocity for each observed frequency. The cube is built with a better spectral resolution (set to 100 m s^{−1} for all models) than the observations, but the predicted spectra are resampled at the same spectral resolution as that of the observations. We carefully take into account the different telescopes source pointings in the convolution by using the appropriate positions given in Section 2.

All HCO⁺ and its isotopologues (except D¹³CO⁺) collision files have been taken from the Leiden Atomic and Molecular Database¹ (LAMDA; Schöier et al. 2005). For each molecule, we have updated the spectroscopic values implemented in these collision files with the newest spectroscopic data taken from the Cologne Database for Molecular Spectroscopy² (CDMS; Müller et al. 2005). The collisional rates are taken from Flower (1999) and were calculated for

¹<http://home.strw.leidenuniv.nl/~moldata/>

²<http://www.astro.uni-koeln.de/cdms/>

Table 1. Parameters for the observed HCO^+ , H^{13}CO^+ , HC^{18}O^+ , DCO^+ , and D^{13}CO^+ lines.

Molecule	Transition	Freq.	E_{up}	A_{ij}	rms	V_{LSR}^a	FWHM ^a	T_{mb}^b	$\int T_{\text{mb}} dv^b$	Telescope	Beam size (arcmin)	η_{mb}
	$J_{\text{up}}-J_{\text{low}}$	(GHz)	(K)	(s^{-1})	(mK)	(km s^{-1})	(km s^{-1})	(K)	(K km s^{-1})			
HCO^+	1–0 ^c	89.189	4	4.19×10^{-5}	8.1	—	—	—	15.3 ± 1.69	IRAM	27.8	0.81
	3–2 ^c	267.558	26	1.45×10^{-3}	55.8	—	—	—	44.4 ± 4.44	APEX	23.5	0.75
	4–3 ^c	356.734	43	3.57×10^{-3}	26.1	—	—	—	67.6 ± 6.76	JCMT	13.9	0.64
	6–5	535.062	90	1.25×10^{-2}	11.5	3.52 ± 0.03	2.43 ± 0.08	7.73 ± 0.80	21.1 ± 2.11	HIFI	39.7	0.62
	7–6	624.208	120	2.01×10^{-2}	12.4	3.48 ± 0.02	2.55 ± 0.04	7.85 ± 0.79	21.6 ± 2.16	HIFI	34.0	0.62
	8–7	713.341	154	3.02×10^{-2}	27.7	3.55 ± 0.02	2.86 ± 0.04	6.50 ± 0.65	20.1 ± 2.01	HIFI	29.7	0.65
	9–8	802.458	193	4.33×10^{-2}	37.5	3.70 ± 0.02	3.46 ± 0.04	5.28 ± 0.79	17.9 ± 2.69	HIFI	26.4	0.63
	10–9	891.557	235	5.97×10^{-2}	37.5	3.83 ± 0.01	3.88 ± 0.03	4.42 ± 0.66	15.6 ± 2.34	HIFI	23.8	0.63
	11–10	980.636	282	7.98×10^{-2}	44.6	3.88 ± 0.01	4.27 ± 0.03	3.63 ± 0.54	12.4 ± 1.86	HIFI	21.6	0.64
	12–11	1069.694	334	1.04×10^{-1}	63.3	3.87 ± 0.02	4.41 ± 0.05	2.64 ± 0.53	9.20 ± 1.84	HIFI	19.8	0.64
	13–12	1158.727	389	1.33×10^{-1}	147.2	4.04 ± 0.04	4.77 ± 0.11	2.13 ± 0.43	8.29 ± 1.66	HIFI	18.3	0.59
H^{13}CO^+	1–0	86.754	4	3.85×10^{-5}	6.5	4.17 ± 0.01	2.13 ± 0.21	1.91 ± 0.21	4.13 ± 0.45	IRAM	28.5	0.81
	2–1	173.507	12	3.70×10^{-4}	22.1	4.48 ± 0.03	2.05 ± 0.06	3.74 ± 0.63	7.73 ± 1.31	IRAM	14.3	0.69
	3–2	260.255	25	1.34×10^{-3}	14.2	3.61 ± 0.02	3.04 ± 0.04	3.19 ± 0.54	9.98 ± 1.70	IRAM	9.50	0.53
	4–3	346.998	42	3.29×10^{-3}	22.1	3.52 ± 0.03	2.36 ± 0.06	3.52 ± 0.63	7.65 ± 1.38	JCMT	14.3	0.64
	6–5	520.460	87	1.15×10^{-2}	9.2	4.02 ± 0.02	3.21 ± 0.05	0.35 ± 0.04	1.02 ± 0.10	HIFI	40.8	0.62
	7–6	607.175	117	1.85×10^{-2}	11.2	4.06 ± 0.06	3.00 ± 0.14	0.24 ± 0.04	0.67 ± 0.10	HIFI	35.0	0.62
	8–7	693.876	150	2.78×10^{-2}	22.0	4.18 ± 0.11	3.31 ± 0.27	0.14 ± 0.04	0.29 ± 0.09	HIFI	30.6	0.65
	9–8	780.563	187	3.99×10^{-2}	27.2	—	—	—	< 0.210	HIFI	27.2	0.65
	10–9	870.354	229	5.97×10^{-2}	37.5	3.83 ± 0.01	3.88 ± 0.03	4.42 ± 0.66	15.6 ± 2.34	HIFI	23.8	0.63
HC^{18}O^+	1–0	85.162	4	3.64×10^{-5}	5.9	4.17 ± 0.05	1.96 ± 0.13	0.18 ± 0.03	0.35 ± 0.04	IRAM	29.1	0.81
	2–1	170.323	12	3.50×10^{-4}	19.6	4.34 ± 0.05	1.66 ± 0.12	0.42 ± 0.08	0.70 ± 0.12	IRAM	14.5	0.69
	3–2 ^e	255.479	25	1.27×10^{-3}	9.7	3.57 ± 0.27	2.43 ± 0.71	0.11 ± 0.06	0.28 ± 0.15	IRAM	9.7	0.54
	4–3	340.631	41	3.11×10^{-3}	16.2	3.96 ± 0.08	3.11 ± 0.21	0.36 ± 0.07	1.12 ± 0.20	JCMT	14.5	0.64
	6–5	510.910	86	1.09×10^{-2}	10.6	4.27 ± 0.11	2.31 ± 0.27	0.06 ± 0.04	0.12 ± 0.06	HIFI	41.6	0.62
	7–6	596.034	114	1.75×10^{-2}	13.7	—	—	—	< 0.106	HIFI	35.8	0.62
DCO^+	2–1	144.077	10	2.12×10^{-4}	13.7	4.32 ± 0.01	1.42 ± 0.01	3.57 ± 0.61	5.45 ± 0.93	IRAM	17.2	0.73
	3–2	216.113	21	7.66×10^{-4}	17.8	4.41 ± 0.03	2.91 ± 0.09	1.74 ± 0.30	5.67 ± 0.97	IRAM	11.5	0.62
	4–3	288.144	35	1.88×10^{-3}	8.90	4.20 ± 0.03	2.24 ± 0.06	1.24 ± 0.25	2.87 ± 0.57	APEX	21.8	0.75
	5–4	360.170	52	3.76×10^{-3}	20.9	3.86 ± 0.04	2.51 ± 0.10	1.16 ± 0.21	2.57 ± 0.46	JCMT	13.7	0.64
	7–6	504.200	97	1.06×10^{-2}	10.9	4.02 ± 0.09	3.03 ± 0.22	0.08 ± 0.02	0.22 ± 0.05	HIFI	42.1	0.62
	8–7 ^d	576.202	124	1.59×10^{-2}	9.1	—	—	—	< 0.396	HIFI	36.8	0.62
D^{13}CO^+	2–1	141.465	10	2.00×10^{-4}	11.7	4.38 ± 0.07	1.27 ± 0.16	0.21 ± 0.06	0.27 ± 0.05	IRAM	17.5	0.73
	3–2	212.194	20	7.25×10^{-4}	6.6	4.43 ± 0.26	2.69 ± 0.61	0.08 ± 0.03	0.22 ± 0.04	IRAM	11.7	0.63
	4–3	282.920	34	1.78×10^{-3}	7.10	4.55 ± 0.14	3.05 ± 0.34	0.07 ± 0.02	0.21 ± 0.04	APEX	22.2	0.75
	5–4	353.640	51	3.56×10^{-3}	27.3	—	—	—	< 0.211	JCMT	14.0	0.64

^aThe error bars only correspond to a statistical error estimated from a Gaussian fit.^bThe error bars are calculated following: $\sigma_{\text{tot}} = \sqrt{\sigma_{\text{cal}}^2 + \sigma_{\text{stat}}^2}$ with σ_{cal} the calibration error taken from Caux et al. (2011) and Ceccarelli et al. (2010) and σ_{stat} the statistical error estimated from a Gaussian fit.^cLines showing a strong self-absorption profile.^dTransition blended with CO ($J = 5 \rightarrow 4$).^eTransition badly calibrated (see Caux et al. 2011).

temperatures in the range from 10 to 400 K including energy levels up to $J = 20$ for collisions with H_2 . Since the D^{13}CO^+ file does not exist, we have created it from the CDMS data base by considering that the collisional rates are the same as for DCO^+ .

4 PHYSICAL AND CHEMICAL STRUCTURE

The physical structure of IRAS16293 is very complex with multiple outflows, multiple sources, and an envelope. To reproduce the observed HCO^+ emission and line profiles, we have modelled in 3D the different structures that contribute to the overall emission. For that, we define the physical structure of each component and their respective HCO^+ abundance profile, as described in the following subsections.

4.1 The envelope model

4.1.1 Physical profile

Crimier et al. (2010) have derived the physical structure of the source (H_2 density, gas, and dust temperature profiles of the envelope). This physical profile has been used in several physical and chemical studies of the source (e.g. Hily-Blant et al. 2010; Vastel et al. 2010; Coutens et al. 2012; Bottinelli et al. 2014; Jaber et al. 2014; Wakelam et al. 2014; López-Sepulcre et al. 2015; Majumdar et al. 2016) and we base our physical structure on the same definition. The Shu-like density distribution described by Crimier et al. (2010) is

$$n(r) = n(r_{\text{in}}) \times \left(\frac{r_{\text{in}}}{r}\right)^{1.5} \quad \text{if } r < r_{\text{inf}}, \quad (1)$$

$$n(r) = n(r_{\text{in}}) \times \left(\frac{r_{\text{in}}}{r}\right)^2 \quad \text{if } r > r_{\text{inf}}, \quad (2)$$

where $n(r_{\text{in}})$ is the density at r_{in} , the inner radius of the envelope, and r_{inf} refers to the radius where the envelope begins to collapse, marking a change in the slope of the density profile (Shu 1977). From their best result, Crimier et al. (2010) derived $r_{\text{inf}} = 1280$ au, $r_{\text{in}} = 22$ au, and $n(r_{\text{in}}) = 1.23 \times 10^9 \text{ cm}^{-3}$. Using these parameters and equations (1) and (2), we performed a spline interpolation of the profiles down to 1 au, for the sake of the radiative transfer modelling. The density profiles, gas and dust temperature profiles are shown in the left and middle panels of Fig. 1, respectively. One must note that the presence of multiple sources and protoplanetary discs in the core of the envelope (hot corinos) cannot be taken into account in the DUSTY model of Crimier et al. (2010). Thus, the inner structure of the source (<600 au) is still open to discussions. However, the abundance of HCO⁺ in this region of the envelope does not contribute significantly to the total emission of the line, as discussed in Section 6.1.

The velocity field of the source is based on the standard infall law in which the envelope is free-falling inside r_{inf} , and considered to be static outside (thus the infall velocity is set to 0). Hence, the velocity field is described by the following equations:

$$V_{\text{inf}}(r) = V_{\text{inf}}(r_{\text{in}}) \quad \text{if } r \leq r_{\text{in}}, \quad (3)$$

$$V_{\text{inf}}(r) = \sqrt{\frac{2GM_{\star}}{r}} \quad \text{if } r_{\text{in}} < r < r_{\text{inf}}, \quad (4)$$

$$V_{\text{inf}}(r) = 0 \quad \text{if } r \geq r_{\text{inf}}, \quad (5)$$

where V_{inf} is the infall velocity, G is the gravitational constant, M_{\star} is the mass of the central object, and r is the distance from the central object (see the right-hand panel of Fig. 1). This formalism of the velocity field as already been used in a previous study of the source (Coutens et al. 2012). For IRAS16293, the mass of the source A dominates the system and we set $M_{\star} = 1 M_{\odot}$ (Ceccarelli et al. 2000a,b; Schöier et al. 2002; Pech et al. 2010; Coutens et al. 2012). We have checked that a variation of the mass between 0.8 and 1.5 solar masses only changes line widths by up to 10 per cent. For smaller or larger value, the modelled HCO⁺ lines are too narrow or too broad, respectively. The envelope is supposed to be centred on IRAS16293 A, since it is the more massive component of the binary system.

4.1.2 Chemical modelling of HCO⁺

We have used the gas-grain chemical code NAUTILUS (e.g. Ruaud, Wakelam & Hersant 2016) to estimate the radial abundance profile of HCO⁺ in the envelope of IRAS16293. NAUTILUS computes the evolution of the species' abundances as a function of time in the gas-phase and on grain surfaces. A large number of gas-phase processes are included in the code: bimolecular reactions (between neutral species, between charged species, and between neutral and charged species) and unimolecular reactions, i.e. photoreactions with direct UV photons and UV photons produced by the de-excitation of H₂ excited by cosmic ray particles (Pratap & Tarafdar mechanism), photodesorption, and direct ionization and dissociation by cosmic ray particles. The interactions of the gas phase species with the interstellar grains are sticking of neutral gas-phase species to the grain surfaces, evaporation of the species from the surfaces due to the temperature, the cosmic ray heating and the exothermicity of the reactions at the surface of the grains (a.k.a. chemical desorption).

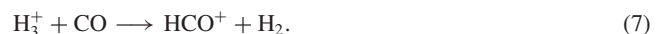
The species can diffuse and undergo reactions using the rate equation approximation at the surface of the grains (Hasegawa, Herbst & Leung 1992). Details on the processes included in the model can be found in Ruaud et al. (2016). Note that we have used NAUTILUS in its two-phase model, meaning that there is no distinction between the surface and the bulk of the mantle of the grains. The gas-phase reactions are based on the `kida2015.uva.2014` network³ (see Wakelam et al. 2015), while the surface reactions are based on the Garrod & Herbst (2006) network. The full network contains 736 species (488 in the gas-phase and 248 at the surface of the grains) and 10 466 reactions (7552 pure gas-phase reactions and 2914 reactions of interactions with grains and reactions at the surface of the grains). For this study, we adopted the initial atomic abundances (with respect to the total proton density n_{H}) given in Hincelin et al. (2011) with an additional atomic abundance of 6.68×10^{-9} for fluorine (Neufeld, Wolfire & Schilke 2005). The carbon and oxygen abundances are, respectively, 1.7×10^{-4} and 3.3×10^{-4} leading to a C/O ratio of ~ 0.5 .

The chemical modelling of the envelope is done in two steps, as explained in Quénard et al. (2017b). Initially, it starts by considering a static 0D parental cloud extended up to $r = 4 \times 10^4$ au with an initial gas temperature varying from 10 to 30 K (see Section 5) and a high visual extinction to prevent any photodissociation to occur. The second step starts with the final abundances of the parental cloud step. In this phase, we consider the 1D physical structure of the envelope, supposed static as a function of time (see Section 6.1). Abundances of species as a function of the radius are output for different ages of the proto-star, up to 1×10^5 yr. The cosmic ray ionization rate ζ is supposed to be the same as the one used for the parental cloud step. The visual extinction in the envelope is a function of the atomic hydrogen column density N_{H} , calculated from the H₂ density profile:

$$A_V = \frac{N_{\text{H}}}{1.59 \times 10^{21} \text{ cm}^{-2}}. \quad (6)$$

We also take into account the additional extinction from the foreground cloud in which we assume that the envelope is embedded (see §1 of Section 6.2).

The chemical reaction network of HCO⁺ depends strongly on H₃⁺ since its primary formation route is



H₃⁺ is formed from H₂ and strongly depends on the cosmic ray (CR) ionization rate ζ :



In Section 6.1, we show the significance of the cosmic ray ionization rate in the abundance profiles of HCO⁺ in the envelope, and hence the contribution of this structure to the total emission of this species.

4.2 The foreground cloud

IRAS16293 is embedded in the remnants of its parental cloud, forming a foreground layer in the line of sight. This cloud has been studied by Coutens et al. (2012) and Wakelam et al. (2014) to analyse the deuteration in the source, and Bottinelli et al. (2014) to investigate

³<http://wakelam2015.obs.u-bordeaux1.fr/networks.html>

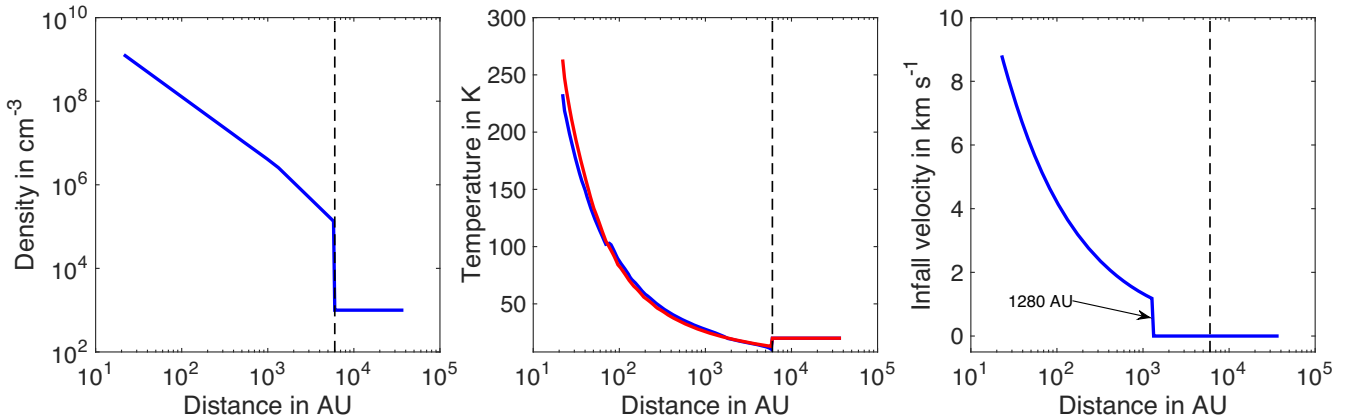


Figure 1. *Left-hand panel:* Density profile of IRAS16293 used in this study as a function of the radius. *Middle panel:* Gas (blue) and dust (red) temperature profiles of IRAS16293 used in this study as a function of the radius. *Right-hand panel:* Absolute value of the radial infall velocity as a function of the radius. In all panels, the black dotted line shows the $R = 6000$ au limit of the foreground cloud.

CH in absorption. Based on these studies, this cloud must be cold ($T_{\text{kin}} \sim 10\text{--}30$ K) and not very dense ($n(\text{H}_2) \sim 10^3\text{--}10^5 \text{ cm}^{-3}$) with an A_V of 1–4, similar to the physical conditions found in diffuse or translucent clouds (Hartquist & Williams 1998). The expected range of the HCO^+ abundance is a few $10^{-10}\text{--}10^{-8}$ [unless stated differently, all abundances in this study are defined with respect to $n(\text{H}_2)$], depending on the temperature and on the degree of ionization of the cloud (Lucas & Liszt 1996; Hartquist & Williams 1998; Savage & Ziurys 2004). The V_{LSR} of the foreground cloud is supposed to be 4.2 km s^{-1} (compared to the $V_{\text{LSR}} = 3.8 \text{ km s}^{-1}$ of IRAS16293), as derived by previous studies (Vastel et al. 2010; Coutens et al. 2012; Bottinelli et al. 2014).

4.3 The outflow model

The observed line shapes and intensities cannot be explained only with the contribution of the envelope of the source, particularly for high upper energy level transitions (e.g. $J_{\text{up}} > 9$). This effect has been also observed by Gregersen et al. (1997) who performed a survey of HCO^+ towards 23 Class 0 proto-stars. They determined from their HCO^+ spectra [using HCO^+ (4–3) and (3–2) transitions] that emission coming from bipolar outflows are contaminating the wings of the line, which might be confused with emission coming from the infalling envelope. Moreover, HCO^+ is a molecule known to trace low-velocity entrained gas of outflows (e.g. Sánchez-Monge et al. 2013).

A young NW-SE outflow (~ 400 yr) has been traced with SiO and CO emission (Rao et al. 2009; Girart et al. 2014) using the SMA interferometer. Rawlings, Taylor & Williams (2000) and Rollins et al. (2014) have shown that young outflows can lead to an enhancement of the HCO^+ abundance in a short period of time. Briefly, the interaction between the jet and/or the outflowing material and the surrounding quiescent (or infalling) gas is eroding the icy mantle of dust grains, desorbing the molecular materials in the gas phase (e.g. H_2O , CO, H_2CO , and CH_3OH). Thanks to the photochemical processing induced by the shock-generated radiation field, this sudden enrichment of the gas-phase molecular abundances leads to the formation of many other molecules, such as HCO^+ . HCO^+ will be then destroyed by dissociative recombination or by interaction with water. Thus, we do not expect a high HCO^+ abundance in old outflows but rather in young ones ($< \text{few hundred years old}$, Rawlings

et al. 2000) such as the NW-SE outflow detected in IRAS16293. Rao et al. (2009) observed H^{13}CO^+ arising from the same region as this NW-SE outflow, but they associated it with rotating material around IRAS16293 A rather than the outflow. Since the direction of this rotating material is roughly the same as the NW-SE outflow, it is more probable that the H^{13}CO^+ emission they observed is due to the recent enhancement of abundance. This conclusion is also supported by more recent H^{13}CO^+ SMA maps presented by Jørgensen et al. (2011; see their fig. 19). Therefore, we have included this outflow in our 3D model together with the envelope.

We have considered an hourglass-like geometry for the outflow, as used by Rawlings et al. (2004) in their study of HCO^+ . This model is based on the mathematical definition given in Visser et al. (2012) implemented in GASS (see Quénard et al. 2017a for more details on the outflow modelling). Rao et al. (2009) and Girart et al. (2014), using SMA interferometric observations, derived the maximum extent of this outflow (8 arcsec), its inclination (44°), dynamical age (~ 400 yr), position angle (145°), and velocity ($V_{\text{outflow}} = 15 \text{ km s}^{-1}$). Density and temperature are not really well constrained, but based on their SiO (8–7) emission, Rao et al. (2009) suggested that this outflow is dense ($n(\text{H}_2) \sim 1 \times 10^7 \text{ cm}^{-3}$) and hot ($T_{\text{kin}} \sim 400$ K). A correlation between SiO and HCO^+ emission in outflows has already been observationally reported in high-mass star-forming regions (Sánchez-Monge et al. 2013); hence, we decided to consider that the HCO^+ emission arises from a region with similar physical properties.

We aim at giving better constraints on the density and temperature of the outflow using all the HCO^+ observations, thus we choose to only vary the gas temperature, the H_2 density, as well as the HCO^+ abundance, all three considered to be constant as a function of the radius as a first approximation.

This outflow is quite young, collimated, and its low velocity suggests that the surrounding envelope is being pushed by the outflowing material. This kind of outflow–envelope interaction has already been observed and studied by Arce & Sargent (2005, 2006) for similar objects. Such interaction between the outflow and the envelope implies that there is no outflow cavity, as suggested by the interferometric observations, so we did not set it in the models. Fig. 2 presents a sketch of the outflow orientation and position in the model with respect to sources A and B.

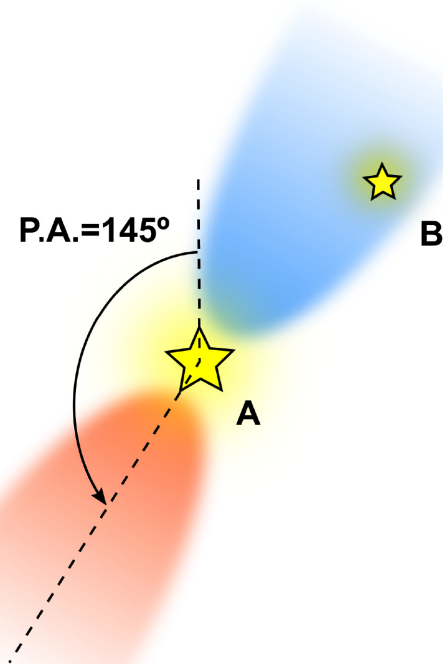


Figure 2. Sketch of the blueshifted (in blue) and redshifted (in red) NW-SE outflow emission. Both sources A and B (separated by 5 arcsec) are drawn but only source A is considered in the modelling.

5 METHODS

One of the strengths of this study resides in the use of the data from the unbiased spectral surveys TIMASSS and CHESS (Section 2), which provides us with a large number of transitions, spanning a wide range of upper energy levels (4–389 K). Since the different structures contained in the physical model of the source span different temperature (and density) conditions, each structure is probed by a different set of transitions. For instance, the emission of the HCO^+ low $J = 1 \rightarrow 0$ transition ($E_{\text{up}} = 4$ K) is more sensitive to the cold foreground cloud conditions, while the $J_{\text{up}} \gtrsim 8$ transitions ($E_{\text{up}} \gtrsim 154$ K) of the same molecule will preferentially help to constrain the outflow physical parameters, but poorly the envelope since the latter is much colder and is therefore contributing less to the total emission of these lines.

All 31 detected transitions of HCO^+ and its isotopologues have been modelled using GASS and LIME. A grid of more than 5000 models have been calculated to constrain the physical properties of the envelope, foreground cloud, and outflow. The range of tested values is shown in Table 2. To derive the best-fitting model, we have compared the predicted line fluxes of all lines with the observed values. Models where all line fluxes are falling within an error bars of 20 per cent with respect to the observed value are also shown in Table 2. These 20 per cent error models are here to show how restrictive the constraints found in our study are (or not) with respect to the best model.

In the following section, we discuss the impact of the input parameters on the line profiles. As said above, each structure (envelope, outflow, foreground cloud) is probed by different HCO^+ transitions, driven by the upper energy level of the transition. Therefore, to simplify the discussion on the impact of the input parameters, we have selected a subset of lines that best represent (visually) the variations

of the parameters of each structure. For the envelope, the HCO^+ (8–7) transition is the most sensitive to the variation of the envelope parameters while for the foreground cloud the low- J HCO^+ (1–0) transition is used and for the outflow the high- J HCO^+ (10–9) is selected.

6 RESULTS AND DISCUSSIONS

The best model parameters we derived following our method are summarized in Table 2. A comparison between the observed line profiles and the best-fitting model for all the studied transitions of HCO^+ is presented in Fig. A1.

6.1 Chemistry of HCO^+ in the envelope

Proto-stellar envelopes are by nature dynamical objects and the time-scale of collapse may change the chemical composition of the envelopes (see Aikawa et al. 2008; Wakelam et al. 2014). The HCO^+ emission however seems to originate from the outer part of the envelope ($\gtrsim 1000$ au). Indeed, at this radius, the gas-phase abundance of H_3^+ is enhanced due to the cosmic ray ionization (see Section 3) and it reacts with CO, increasing the abundance of HCO^+ . In this region, the physical conditions are evolving much more slowly, and, for this reason, the use of a static model to derive the HCO^+ abundance in the envelope rather than a dynamical structure is justified here.

Five different parameters have been separately varied (age, temperature, and density of the parental cloud, cosmic ray ionization rate, and age of the proto-star) to discriminate the impact of the chemical modelling input parameters on the radial abundance profile of HCO^+ . We have then used this radial abundance profile to predict the line emission of HCO^+ in order to compare with observations. We emphasize that the tested models also include the outflow and the foreground cloud structure. The best model (determined following the method described in Section 5) gives a parental cloud evolving for 1×10^5 yr with an initial gas density $n(\text{H}_2) = 3 \times 10^4 \text{ cm}^{-3}$, and a cosmic ray ionization rate of $1 \times 10^{-16} \text{ s}^{-1}$ with the age of the proto-star estimated to be 3.8×10^4 yr. Fig. 3 shows the effect of the variation of the chemical parameters on the radial abundance profile of HCO^+ and Fig. 4 the resulting line profile of the HCO^+ (8–7) transition.

Age of the parental cloud. It is well constrained to be $\leq 3 \times 10^5$ yr since for older ages the amount of HCO^+ drops drastically (see the top panels of Fig. 3); therefore, the predicted HCO^+ emission is weaker by more than 20 per cent compared to the observations (see top panels of Fig. 4).

H_2 density of the parental cloud. It is poorly constrained but a higher value of the H_2 density leads to a lower abundance in the external part of the envelope (see the middle panels of Figs 3 and 4). A smaller abundance in this region of the envelope reduces the self-absorption feature of low upper energy transitions ($J_{\text{up}} < 4$). If the density is not too high ($\leq 1 \times 10^5 \text{ cm}^{-3}$), the HCO^+ abundance varies by less than ~ 10 per cent at 2000 au, keeping the integrated flux of the lines within our threshold of 20 per cent.

Kinetic temperature of the parental cloud. A variation of this parameter does not change significantly the resulting HCO^+ abundance profile (and hence the line profiles) so it was arbitrarily fixed to 10 K, according to constraints given by previous studies (e.g. Bottinelli et al. 2014; Wakelam et al. 2014).

Cosmic ray ionization rate. The ionization rate is strongly constrained by the chemical modelling, since it drastically affects the

Table 2. Range of physical properties varied in this study.

Physical properties	Tested range	Best-fitting value	20 per cent error bar
Age of the parental cloud	10^5 – 10^6 yr	1×10^5 yr	$\leq 3 \times 10^5$ yr
$n(\text{H}_2)_{\text{parental cloud}}$	1×10^4 – $3 \times 10^5 \text{ cm}^{-3}$	$3 \times 10^4 \text{ cm}^{-3}$	$\leq 1 \times 10^5 \text{ cm}^{-3}$
$T_{\text{parental cloud}}$	5–15 K	10 K	None
ζ_{envelope}	1×10^{-17} – $1 \times 10^{-16} \text{ s}^{-1}$	$1 \times 10^{-16} \text{ s}^{-1}$	$\geq 5 \times 10^{-17} \text{ s}^{-1}$
Age of the proto-star	up to 10^5 yr	4×10^4 yr	$\geq 2 \times 10^4$ yr
$n(\text{H}_2)_{\text{foreground}}$	5×10^2 – $3 \times 10^5 \text{ cm}^{-3}$	$2 \times 10^3 \text{ cm}^{-3}$	5×10^2 – $1 \times 10^4 \text{ cm}^{-3}$
$T_{\text{kin, foreground}}$	10–30 K	20 K	None
$X(\text{HCO}^+)_{\text{foreground}}$	5×10^{-11} – 1×10^{-6}	1×10^{-8}	1×10^{-9} – 1×10^{-7}
$n(\text{H}_2)_{\text{outflow}}$	1×10^6 – $1 \times 10^8 \text{ cm}^{-3}$	$5.5 \times 10^6 \text{ cm}^{-3}$	$(4\text{--}7) \times 10^6 \text{ cm}^{-3}$
$T_{\text{kin, outflow}}$	100–500 K	200 K	180–220 K
$X(\text{HCO}^+)_{\text{outflow}}$	1×10^{-10} – 1×10^{-7}	4×10^{-9}	$(3\text{--}5) \times 10^{-9}$

Notes. Top panel: Parameters of the envelope. Middle panel: Parameters of the foreground cloud.

Bottom panel: Parameters of the outflow.

amount of HCO^+ in the envelope. A lower cosmic ray ionization rate reduces the amount of HCO^+ (see the bottom panels of Fig. 3) produced throughout the source as well as the intensity of the lines (see the bottom panels of Fig. 4). A rate larger than $\sim 5 \times 10^{-17} \text{ s}^{-1}$ is necessary, otherwise intensities of the modelled lines are below the 20 per cent limit. The rate is higher than the standard value of $1.3 \times 10^{-17} \text{ s}^{-1}$ found in the solar neighbourhood but the ρ Ophiuchus cloud complex is known for its high cosmic ray rate (Hunter et al. 1994). This value is also consistent with previous studies reported for IRAS16293 (e.g. Doty, Schöier & van Dishoeck 2004; Bottinelli et al. 2014).

Age of the proto-star. At older proto-stellar age, a drop in the HCO^+ radial abundance arises at ~ 2000 au (caused by CO being depleted on to grain surfaces), leading to weaker self-absorption of high- J lines. Hence, the line profiles are slightly more compatible with the observations for higher proto-star ages than lower ones. However, from Fig. 4, it is difficult to give any stringent constraints on the age of the source. Taking into account the fluxes of all HCO^+ lines, we derived a lower limit of $\sim 2 \times 10^4$ yr. This age is compatible with recent studies performed towards this source (Majumdar et al. 2016; Quénard et al. 2018).

We also would like to emphasize that the contribution of the envelope to the emission of HCO^+ clearly does not dominate (see Section 6.3); therefore, it is difficult to constrain the chemical input parameters. None the less, some parameters such as the cosmic ray ionization rate or the age of the parental cloud have an important impact on the abundance profile of HCO^+ , and hence on the resulting line profiles, and it is possible to give good constraints on their value. For the density and temperature of the parental cloud as well as the age of the proto-star, no stringent conclusions can be drawn because the effects of these parameters on the line profiles are poorly constrained by the observations.

Finally, the structure of IRAS16293, as revealed by numerous interferometric observations, is in reality much more complicated because it is not homogeneously distributed and peak emissions of some species may occur in a specific region of the source and it can be hardly modelled, even in 3D. This effect has already been observed by e.g. Jørgensen et al. (2011) and it can play an important role in the emission seen with single-dish telescopes. It can explain the difference we get between the predicted model and the observation for optically thin molecules such as HC^{18}O^+ or D^{13}CO^+ . Such effects can also explain the excess in emission seen at red velocities for the HCO^+ (1–0) transition that we struggle to perfectly reproduce (see the following section).

6.2 Physical parameters of the foreground cloud

The best model parameters of the foreground cloud are $n(\text{H}_2)_{\text{foreground}} = 2 \times 10^3 \text{ cm}^{-3}$, $T_{\text{kin, foreground}} = 20$ K, and $X(\text{HCO}^+)_{\text{foreground}} = 1 \times 10^{-8}$. Using equation (6), we derive $A_V \simeq 1.2$ for a supposed foreground cloud depth of 3×10^4 au. All three parameters have been varied at the same time to determine the best fit.

Fig. 5 presents the emission of the HCO^+ (1–0) transition for different models varying the foreground cloud physical parameters. One can note that the emission of this transition is clearly sensitive to the foreground cloud density and abundance, despite the short range of values shown in this figure. The reference model (in green) is the foreground cloud best-fitting parameters (see Table 2) and for each panel we vary one of the parameters only and we fix the other two to the best-fitting value to ease the visualization of the impact of the parameter on the resulting line emission.

H_2 density of the foreground cloud. We have tried several densities ranging from $\sim 1 \times 10^3$ to $\sim 1 \times 10^5 \text{ cm}^{-3}$ as suggested by Coutens et al. (2012) for this region combined with several kinetic temperature and molecular abundances. The density we derive ($n(\text{H}_2)_{\text{foreground}} = 2 \times 10^3 \text{ cm}^{-3}$) is lower than the one used by Bottinelli et al. (2014) and Wakelam et al. (2014) ($n(\text{H}_2)_{\text{foreground}} = 1 \times 10^4 \text{ cm}^{-3}$), but these two studies only tested two different densities ($n(\text{H}_2)_{\text{foreground}} = 1 \times 10^4$ and $1 \times 10^5 \text{ cm}^{-3}$). By varying the abundance and density at the same time, we have found a degeneracy between the two parameters. It means that a viable solution can be found with a higher density if the abundance is lower (and vice versa). In any case, we have derived that for a density higher than $n(\text{H}_2)_{\text{foreground}} = 1 \times 10^4 \text{ cm}^{-3}$ and for any abundance value, the HCO^+ (1–0) transition is not self-absorbed enough (absorption depth higher by a factor of 20 per cent compared to the observations). This strongly constrains the density of the foreground cloud and its visual extinction.

Kinetic temperature of the foreground cloud. Using the constraint obtained by Bottinelli et al. (2014) and Wakelam et al. (2014), who determined the kinetic temperature to be ≤ 30 K (see Section 4.2), we tested values in the range of 10–30 K. The line profiles do not change significantly (less than 5 per cent compared to one another) within this range, so we arbitrarily set the best model value to 20 K.

Abundance of the foreground cloud. The HCO^+ abundance of 1×10^{-8} we obtain is consistent with the results predicted by Hartquist & Williams (1998) and Savage & Ziurys (2004) at low A_V for diffuse or translucent clouds. It is ~ 2 times higher than the

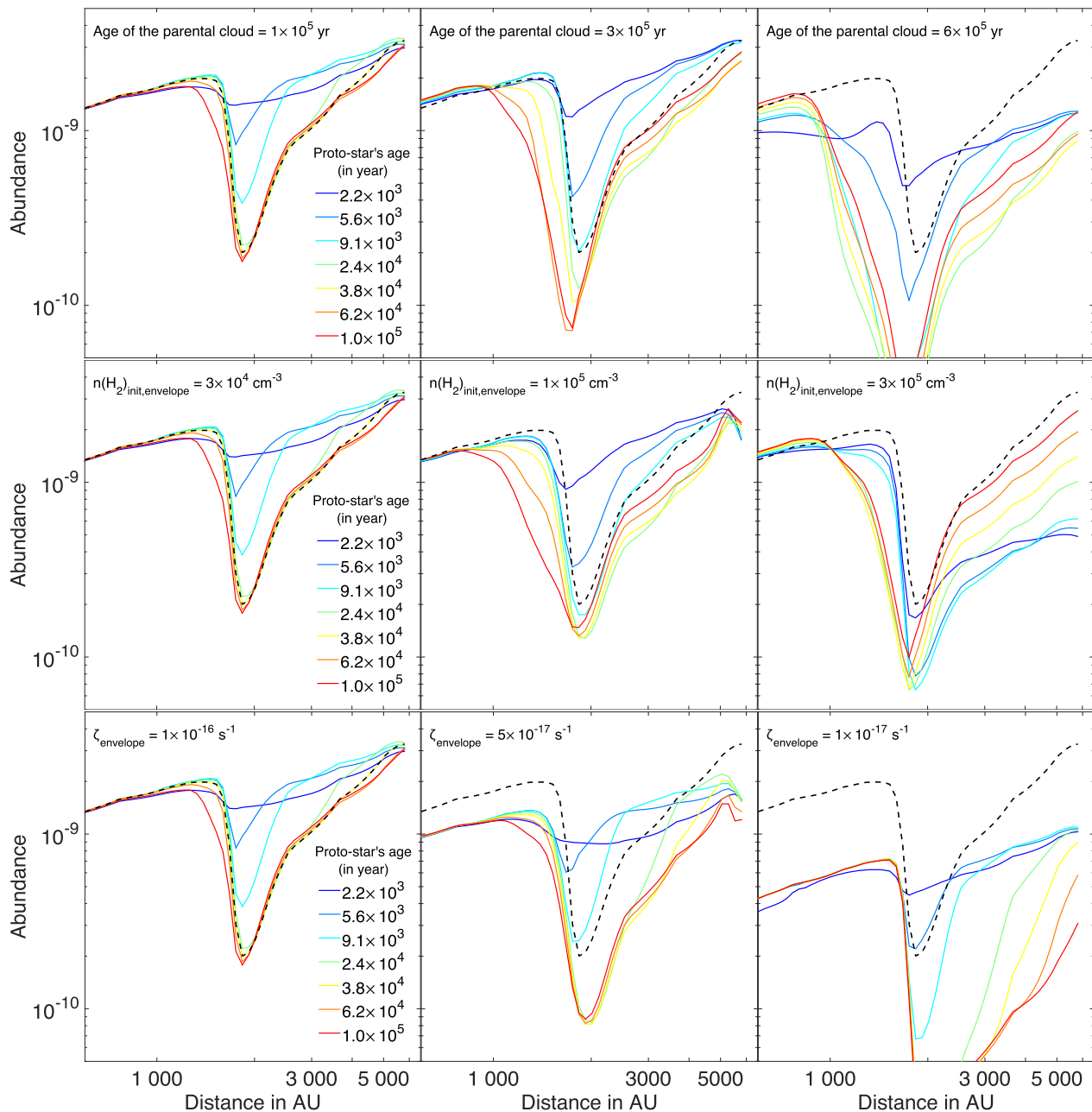


Figure 3. Variation of the abundance profile of HCO^+ determined by NAUTILUS as a function of the radius for different ages of the proto-star and different set of input chemical parameters. The best-fitting (age of the parental cloud = 1×10^5 yr, $n(\text{H}_2) = 3 \times 10^4 \text{ cm}^{-3}$, cosmic ray ionization rate = $1 \times 10^{-16} \text{ s}^{-1}$, and age of the proto-star = 3.8×10^4 yr) is shown in black dashed lines. *Top panels:* Variation of the age of the parental cloud (from left to right): 1×10^5 , 3×10^5 , and 6×10^5 yr. *Middle panels:* Variation of the initial H_2 density in the parental cloud (from left to right): 3×10^4 , 1×10^5 , and $3 \times 10^5 \text{ cm}^{-3}$. *Bottom panels:* Variation of the cosmic ray ionization rate (from left to right): 1×10^{-16} , 5×10^{-17} , and $1 \times 10^{-17} \text{ s}^{-1}$.

observed value of $[3-6] \times 10^{-9}$ derived by Lucas & Liszt (1996) in different diffuse clouds, which is a good agreement. Unfortunately, as mentioned above, there is a degeneracy between the H_2 density and the HCO^+ abundance, limiting the constraints we can give to the HCO^+ abundance ($1 \times 10^{-9} - 1 \times 10^{-7}$).

Finally, we emphasize that none of our models satisfactorily fits the observations very well near the +5 emission and the +4 km s^{-1} dip. Indeed, the HCO^+ (1–0) transition has a very low upper energy level (4 K) and it can be easily excited in cold conditions. As shown above, the foreground cloud physical conditions are crucial to explain the emission of this line, but in order to reduce the

number of free parameters, we have simply considered constant physical conditions in this cloud. Further investigations (beyond the scope of this work) of the temperature and density profiles in this environment may help to recover the observed line shape.

6.3 Physical parameters of the outflow

The best model parameters of the outflow are $n(\text{H}_2)_{\text{outflow}} = 5.5 \times 10^6 \text{ cm}^{-3}$, $T_{\text{kin, outflow}} = 200 \text{ K}$, and $X(\text{HCO}^+)_{\text{outflow}} = 4 \times 10^{-9}$. All three parameters have been varied at the same time to determine the best fit.

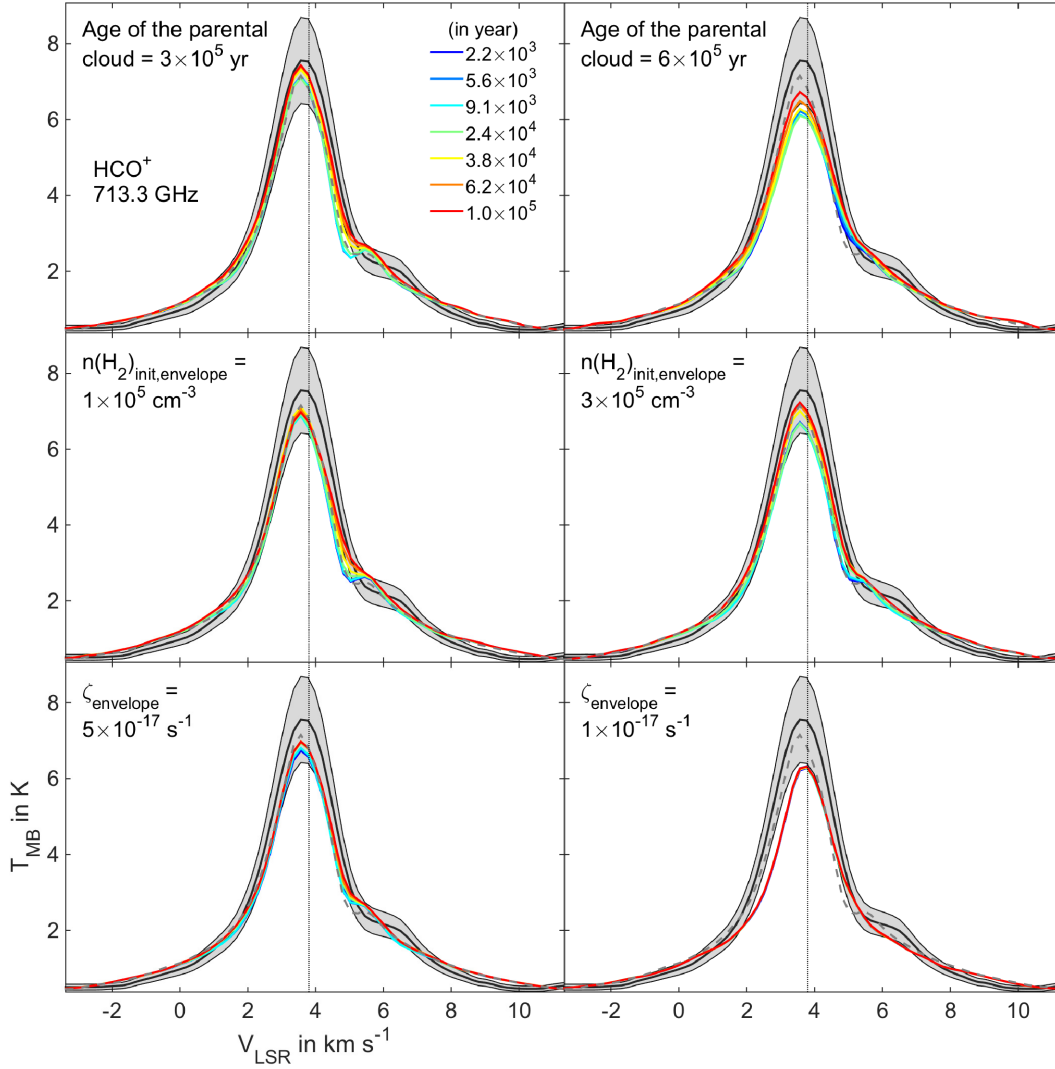


Figure 4. Line profiles of the HCO^+ (8–7) transition for different abundance profiles determined by NAUTILUS for different ages of the proto-star and different sets of input chemical parameters (shown in the middle and right-hand panels of Fig. 3). The best-fitting model is shown in grey dashed lines. The grey area shows a 20 percent error area with respect to the observation (black solid line). The vertical black dotted line shows the supposed $V_{\text{LSR}} = 3.8 \text{ km s}^{-1}$ of IRAS16293. *Top panels:* Variation of the age of the parental cloud (from left to right): 3×10^5 and 6×10^5 yr. *Middle panels:* Variation of the initial H_2 density in the parental cloud (from left to right): 1×10^5 and $3 \times 10^5 \text{ cm}^{-3}$. *Bottom panels:* Variation of the cosmic ray ionization rate (from left to right): 5×10^{-17} and $1 \times 10^{-17} \text{ s}^{-1}$.

Fig. 6 shows the emission of the HCO^+ (10–9) transition for different models varying the outflow physical parameters. As for the foreground cloud, the emission is clearly sensitive to the outflow density and abundance, even for the short range of parameters presented here. Plots shown in Fig. 6 are presented the same way as for the foreground cloud (see §2 of Section 6.2).

H_2 density of the outflow. A similar degeneracy as the one found for the foreground cloud has been obtained for the outflow, between density and abundance. This effect limits the constraints we can give on these two parameters. None the less, to reduce the degeneracy, we have considered previous constraints on the density derived by Rao et al. (2009) and Girart et al. (2014) for the same object ($n(\text{H}_2) \sim 1 \times 10^7 \text{ cm}^{-3}$). Doing so and by varying the abundance and density at the same time, we determined a local minimum around the value of $5.5 \times 10^6 \text{ cm}^{-3}$. A little variation of the density by a factor of ~ 30 percent around this minimum leads to a difference $\gtrsim 20$ percent in the predicted line fluxes, compared to the

observations (see the left-hand panel of Fig. 6). Since this minimum (i) can be constrained by our observations and (ii) is consistent with previous observations, we decided to only consider it in our results.

Kinetic temperature of the outflow. A lower kinetic temperature ($< 180 \text{ K}$) decreases by ~ 6 per cent the emission of high upper energy level lines since the gas is not hot enough to excite these transitions. On the contrary, a higher kinetic temperature ($> 220 \text{ K}$) will increase the line emission by a similar factor. This effect is even more visible for J_{up} higher than the HCO^+ (10–9) transition shown in Fig. 6. For instance, for the HCO^+ (13–12) transition, this factor can reach a value of up to ~ 50 per cent, showing how sensitive these lines are to the kinetic temperature.

Abundance of the outflow. The HCO^+ abundance is hardly constrained due to the degeneracy with the density. However, considering the local minimum of the density, we infer a best-fitting HCO^+ abundance of $\sim 4 \times 10^{-9}$. This value is consistent with the expected enhancement of HCO^+ in outflows described in Section 4.3.

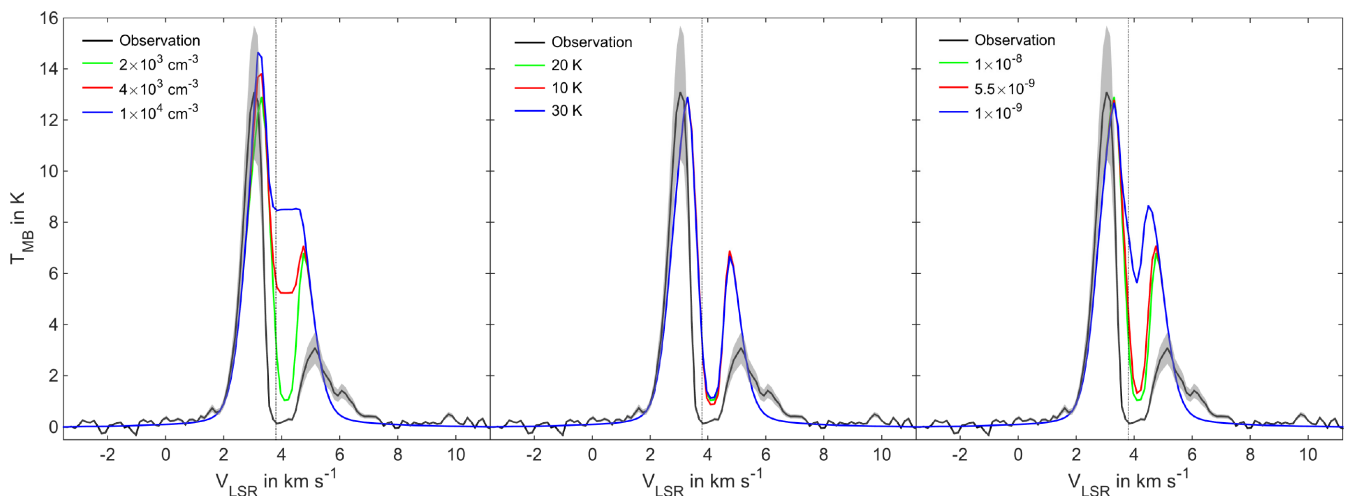


Figure 5. Line profiles of the HCO⁺(1–0) transition for different input parameters of the foreground cloud structure. The grey area shows a 20 per cent error area with respect to the observation (black solid line). The vertical black dotted line shows the supposed $V_{\text{LSR}} = 3.8 \text{ km s}^{-1}$ of IRAS16293. The reference model (in green) is the best fit with $n(\text{H}_2)_{\text{foreground}} = 2 \times 10^3 \text{ cm}^{-3}$, $T_{\text{kin,foreground}} = 20 \text{ K}$, and $X(\text{HCO}^+)_{\text{foreground}} = 1 \times 10^{-8}$. *Left-hand panel:* Variation of the H₂ density of the foreground cloud. *Middle panel:* Variation of the kinetic temperature of the foreground cloud. *Right-hand panel:* Variation of the HCO⁺ abundance of the parental cloud.

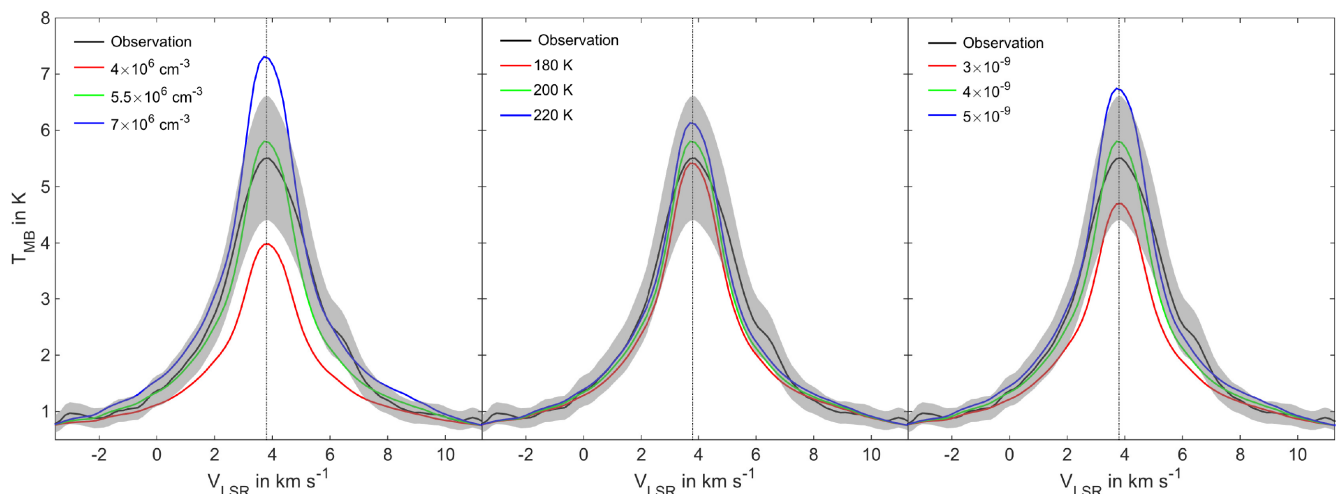


Figure 6. Line profiles of the HCO⁺(10–9) transition for different input parameters of the foreground cloud structure. The grey area shows a 20 per cent error area with respect to the observation (black solid line). The vertical black dotted line shows the supposed $V_{\text{LSR}} = 3.8 \text{ km s}^{-1}$ of IRAS16293. The reference model (in green) is the best fit with $n(\text{H}_2)_{\text{outflow}} = 5.5 \times 10^6 \text{ cm}^{-3}$, $T_{\text{kin,outflow}} = 200 \text{ K}$, and $X(\text{HCO}^+)_{\text{outflow}} = 4 \times 10^{-9}$. *Left-hand panel:* Variation of the H₂ density of the outflow. *Middle panel:* Variation of the kinetic temperature of the outflow. *Right-hand panel:* Variation of the HCO⁺ abundance of the outflow.

The outflow is the dominant structure in inner regions (< 8 arc-sec) for high- J transitions and it largely contributes to the total emission since the envelope temperature is too low ($\sim 50 \text{ K}$) to reproduce alone the emission of these lines. Moreover, when the envelope temperature is high enough ($\sim 150 \text{ K}$ at $\sim 40 \text{ au}$), HCO⁺ is destroyed by recombination with H₂O and the HCO⁺ abundance becomes so low ($\sim 1 \times 10^{-14}$) that it cannot participate in the emission of these high- J transitions. This conclusion is highlighted in Fig. 7, where the contribution of the envelope and the outflow to the total emission of the HCO⁺ (8–7) transition is shown, considering the physical parameters of the best-fitting model. From this figure, it is clear that the contribution of the envelope (in green) to the total emission of HCO⁺ transitions is rather small (especially for high- J transitions). The outflow contribution (in red) clearly dominates the total emission (shown in blue), proving the importance of the out-

flow structure to the emission of high- J HCO⁺ lines. This statement cannot be as easily drawn for lower- J lines, where the emission is a result of the three structures.

We have compared our outflow results with the L1157 molecular outflow and especially with the B1 shock region. The abundance of HCO⁺ in this region has been determined by Bachiller & Pérez Gutiérrez (1997) and Podio et al. (2014). In their case, they do not derive any evident enhancement of HCO⁺ with respect to the dense core value (Podio et al. 2014). This conclusion is consistent with previous observations towards this object (Hogerheijde et al. 1998; Tafalla et al. 2010). From the theoretical studies of Rawlings et al. (2004) and Rollins et al. (2014), it is shown that after an age of a few hundred years and especially after $\sim 500 \text{ yr}$ the HCO⁺ abundance drastically drops in an outflow, and that no enhancement of its abundance with respect to the surrounding en-

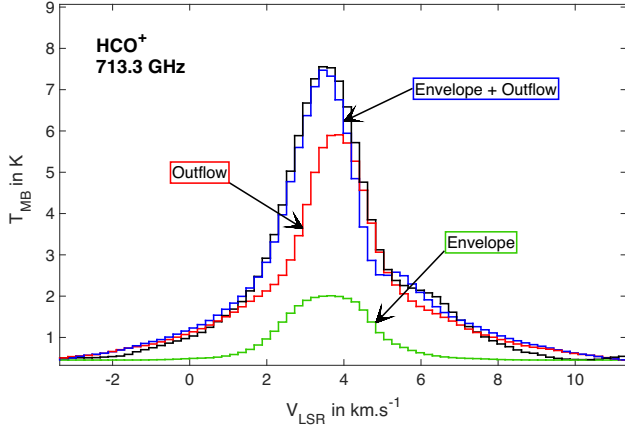


Figure 7. Line profile of the $\text{HCO}^+(8-7)$ transition given by the radiative transfer modelling considering the best-fitting parameters of the envelope (in green) and the outflow (in red) structure and for the envelope + outflow together (in blue). For the blue curve, the radiative transfer modelling is performed with both the outflow and envelope structure in the 3D model, thus the line profile is different from a simple summation of the red and green curves. The observed line profile is plotted in black.

Table 3. Outflow and envelope physical properties.

Physical property	Value
Outflow mass, M_{out}	$0.02 M_{\odot}$
Outflow momentum, P	$0.15 M_{\odot} \text{ km s}^{-1}$
Outflow energy, E	$1.54 \times 10^{43} \text{ erg}$
Outflow mass rate, \dot{M}_{out}	$6.72 \times 10^{-5} M_{\odot} \text{ yr}^{-1}$
Outflow force, F_{out}	$5.04 \times 10^{-4} M_{\odot} \text{ km s}^{-1} \text{ yr}^{-1}$
Mechanical luminosity, L_{out}	$0.42 L_{\odot}$
Dynamical time, t_{dyn}	303 yr
Envelope mass, M_{env}	$2.04 M_{\odot}$
Infall mass rate, \dot{M}_{inf}	$1.92 \times 10^{-4} M_{\odot} \text{ yr}^{-1}$

Note. The envelope mass has been determined from the H_2 density profile and is in agreement with the value given in Crimier et al. (2010).

velope is expected at older ages. This conclusion is in agreement with the observation of L1157-B1 for which the inferred shock age is $t_{\text{shock}} \sim 2000 \text{ yr}$. However, in our case, the estimated dynamical age of the young NW-SE outflow is estimated to be $\sim 400 \text{ yr}$ which is approximately the age for which we expect the abundance to start decreasing. This might be the case here, since the outflow abundance we derive $[\text{X}(\text{HCO}^+)_{\text{outflow}} \sim 4 \times 10^{-9}]$ is roughly the same as the peak abundance of $\text{X}(\text{HCO}^+)_{\text{envelope}} \sim 2 \times 10^{-9}$ we derive for the envelope.

The ranges of outflow density and temperature we obtain in our study are consistent, within a factor of 2, with Rao et al. (2009) and Girart et al. (2014). However, fitting several HCO^+ transitions, we provide a better estimation of the outflow physical conditions, particularly for the kinetic temperature.

Using the outflow physical parameters derived from our modelling, we have calculated several outflow properties (momentum, energy, dynamical age, outflow mass rate, momentum rate, and mechanical luminosity, see Table 3) based on the definition given in Dierickx et al. (2015). The outflow mass is directly extracted from the physical model using $M_{\text{out}} = \mu m_{\text{H}} n(\text{H})_{\text{outflow}} V_{\text{outflow}}$, with $\mu = 2.35$ the mean molecular weight of the gas, m_{H} the mass of the hydrogen atom, $n(\text{H})_{\text{outflow}} = 1.1 \times 10^7 \text{ cm}^{-3}$ the outflow H density, and V_{outflow} the volume of the outflow. The dynamical age derived

from our model ($\sim 300 \text{ yr}$) is close to the value found by Girart et al. (2014) ($\sim 400 \text{ yr}$) from $\text{CO}(3-2)$ observations. However, the outflow mass, mass rate, and momentum rate we derive are ~ 2 orders of magnitude higher than their values. We infer that this difference is due to the different methods used to compute these quantities, derived from the accurate outflow volume and density directly extracted from our model compared to the estimate of Girart et al. (2014) derived from CO line brightness. Finally, we estimated the infall rate of the surrounding envelope assuming spherical symmetry (Pineda et al. 2012): $\dot{M}_{\text{inf}} = 4\pi r_{\text{in}}^2 n_{\text{in}} \mu m_{\text{H}} V_{\text{in}}$, where r_{in} (1280 au) is the radius at which the infall velocity is V_{in} (1.18 km s^{-1}) with a density n_{in} ($2.83 \times 10^6 \text{ cm}^{-3}$). We compare this value to the outflow mass rate and we find $\dot{M}_{\text{out}}/\dot{M}_{\text{inf}} = 0.35$. This value is consistent with the typical ejection over accretion ratio of 0.1–0.3 found in young stellar objects (Shu et al. 1988; Richer et al. 2000; Beuther et al. 2002; Zhang et al. 2005).

6.4 Fractionation

To reproduce the line emission of the HCO^+ isotopologues, we varied the different isotopic ratios. We set a step of 10 for $^{16}\text{O}/^{18}\text{O}$ and a step of 1 for $^{12}\text{C}/^{13}\text{C}$, and explored ranges of [300–800] and [30–80], i.e. bracketing typical local ISM values (Wilson & Rood 1994; Bensch et al. 2001). The $^{12}\text{C}/^{13}\text{C}$ and $^{16}\text{O}/^{18}\text{O}$ best ratios we derived in this study are consistent with values found in the ISM (Wilson & Rood 1994) and for the ρ Ophiuchus cloud (Bensch et al. 2001). The following error bars are given for a 20 per cent difference between the modelled and observed line fluxes.

A constant $^{16}\text{O}/^{18}\text{O} = 460 \pm 50$ ratio is sufficient to reproduce the HC^{18}O^+ observations within a difference of 20 per cent on the line fluxes. Note that the HC^{18}O^+ transition at 255.5 GHz has been ignored in the error calculation due to a bad calibration of the IRAM 30 m observations, as suggested by Caux et al. (2011). This ratio is in good agreement with the typical ratio of 560 ± 25 observed in the ISM (Wilson & Rood 1994). Smith et al. (2015) have determined a $^{16}\text{O}/^{18}\text{O}$ in the ρ Ophiuchus region for different Class I and II objects. From their result (see their table 6), one can note that the ratio increases for more evolved objects, up to a few thousands. In the case of IRS 63, a Class I object, they obtained $^{16}\text{O}/^{18}\text{O} = 690 \pm 60$. Since IRAS16293 is a Class 0, we might expect a lower ratio, in agreement with our finding.

For the $^{12}\text{C}/^{13}\text{C}$ ratio, we derive 51 ± 5 , slightly lower (but still consistent within the error bars) than the value of 65 ± 11 found by Bensch et al. (2001) in the core C of the ρ Ophiuchus molecular cloud, $\sim 2 \text{ deg}$ away from IRAS16293.

While there is no evidence for varying $^{12}\text{C}/^{13}\text{C}$ and $^{16}\text{O}/^{18}\text{O}$ ratios in proto-stellar envelopes, it is not the case for the H/D ratio, whose value is found to be different in different parts of the envelope (e.g. Coutens et al. 2012). This can be explained by the fact that, at low temperature ($T < 30 \text{ K}$) and low densities ($n(\text{H}_2) < 10^5 \text{ cm}^{-3}$), DCO^+ is enhanced, increasing rapidly the fractionation of HCO^+ (Dalgarno & Lepp 1984; Roberts & Millar 2000). Because of the lack of observational constraints on the radial profile of the H/D ratio across the envelope, we decided to use a pragmatic approach and to consider an ad hoc linear law.

For the external part of the envelope, we fixed $\text{H}/\text{D} = 20$, the value derived by Coutens et al. (2012) for the foreground cloud using water lines ($\text{HDO}/\text{H}_2\text{O} \sim 4.8 \text{ per cent}$). To the best of our knowledge, this is the only estimated value of deuterium fractionation in this region of IRAS16293. In the inner region of the envelope, close to the hot corinos, the H/D ratio varies around $\sim [30-100]$ for various complex organic molecules (Coutens et al. 2016; Jørgensen

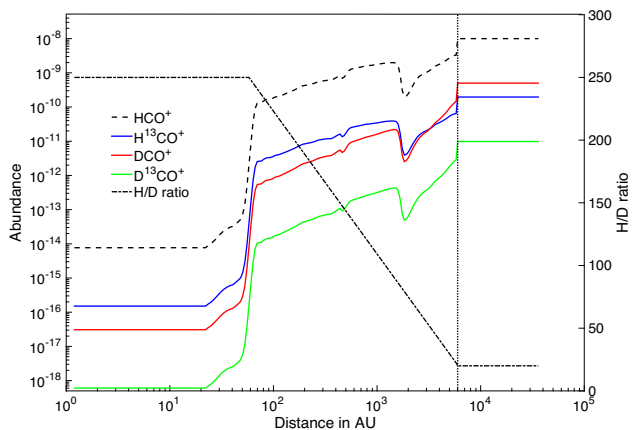


Figure 8. *Left axis:* Abundance profile of HCO⁺ (black dashed line) as a function of the radius compared to the H¹³CO⁺ (blue), DCO⁺ (red), and D¹³CO⁺ (green) one. *Right axis:* D/H ratio used in this study (black dash-dotted line). The vertical black dotted line shows the $R = 6000$ au limit of the foreground cloud.

et al. 2016), but Persson, Jørgensen & van Dishoeck (2013) and Persson et al. (2014) derived a higher value (~ 1000) for water in the hot corino of IRAS16293 and other low-mass proto-stars. We have tried several inner value ranging between 30 and 1000 (with a step of 10), and we found that $H/D = 250 \pm 40$ gave the best match between model and observations.

For the envelope of IRAS16293, Loinard et al. (2000, 2001) found a value of 100 from column densities derived using only one low upper energy level transition of H¹³CO⁺ and DCO⁺. Our values, between 20 and 250, depending on the radius are consistent with this ratio. More recently Koumpia et al. (2017) derived in NGC1333 IRAS 4A, an other Class 0 proto-star, a similar ratio of 100 in the proto-stellar envelope, also in agreement with our values in the envelope of IRAS16293.

Finally, we want to emphasize that the outflow does not contribute much for the total emission of HC¹⁸O⁺ and DCO⁺. However, it might contribute significantly for H¹³CO⁺, as shown in the maps from Jørgensen et al. (2011; see their fig. 19). Moreover, since we are using only pointed observations (and not maps), it is hard to draw conclusions on the possible inhomogeneities and substructures of the envelope, possibly affecting the emission of the HC¹⁸O⁺ and DCO⁺ lines (see also Section 6.1).

The HCO⁺, H¹³CO⁺, DCO⁺, and D¹³CO⁺ abundance profiles are plotted in Fig. 8 alongside with the H/D ratio.

6.5 Ionization degree in the envelope

We have determined the ionization degree $x(e)$ in the envelope of IRAS16293 using the results given by the chemical modelling. The ionization degree (abundance of electron as a function of the radius) is shown in the top panel of Fig. 9, alongside the abundance of HCO⁺ and two other important ions in the envelope (N₂H⁺ and H₃⁺). HCO⁺ is the main ion in the envelope until ~ 1500 au and we have $x(e) \simeq X(\text{HCO}^+)$, as expected when CO is not depleted (Caselli et al. 2002b). The ionization degree we find is

$$10^{-8.9} \lesssim x(e) \lesssim 10^{-7.9}. \quad (10)$$

From the ionization degree, we have been able to determine the relationship between $x(e)$ and $n(\text{H}_2)$, using the envelope density

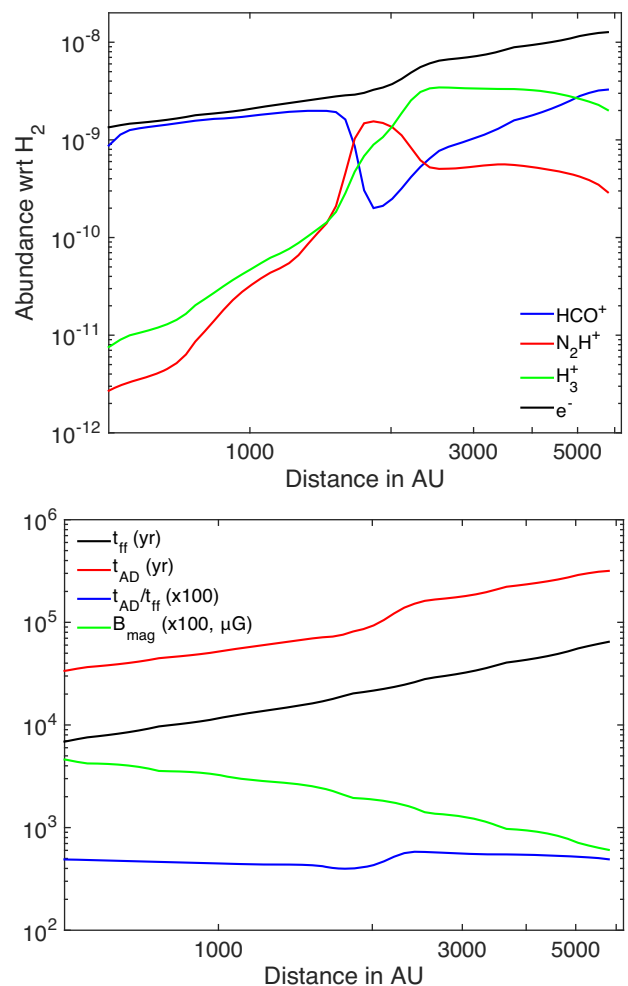


Figure 9. *Top panel:* Abundance as a function of the radius for electrons (in black) and three main ions (HCO⁺, N₂H⁺, and H₃⁺, in colours) in the envelope, extracted from the chemical modelling. *Bottom panel:* Free-fall (in black) and ambipolar diffusion (in red) time-scales, ratio of the two time-scales (in blue, multiplied by 100), and magnetic field (in green, multiplied by 100) across the envelope.

profile (see Section 4.1). By fitting a power-law profile, we find

$$x(e) = 3.04^{+0.60}_{-0.59} \times 10^{-6} n(\text{H}_2)^{-0.460 \pm 0.015}. \quad (11)$$

Our value is ~ 5 times lower than the standard value of $x(e) = 1.5 \times 10^{-5} n(\text{H}_2)^{-0.5}$ determined by McKee (1989; see also Basu & Mouschovias 1994). This means that the ionization balance in the envelope is not dictated by cosmic rays alone (McKee 1989). Caselli et al. (2002c) also came to this conclusion in the evolved cold dense core L1544 and they inferred that the depletion of metals is the cause of the reduced ionization degree (Caselli et al. 1998), which might be also the case here. Interestingly, our $x(e) - n(\text{H}_2)$ relation is close to the one obtained by Caselli et al. (2002b) in L1544, indicating that the physical conditions in the envelope of IRAS16293 may resemble those of a previous pre-stellar phase, which is consistent with our choice to consider the physical conditions in the envelope static in Section 6.1.

From the ionization degree, we have determined the ambipolar diffusion time-scale t_{AD} (Spitzer 1978; Shu et al. 1987):

$$t_{\text{AD}}(\text{yr}) = 2.5 \times 10^{13} x(e). \quad (12)$$

In our case, $3.4 \times 10^4 \text{ yr} \lesssim t_{\text{AD}} \lesssim 3.2 \times 10^5 \text{ yr}$ (see the bottom panel of Fig. 9). We compared this value to the free-fall time-scale t_{ff} of the envelope, given by

$$t_{\text{ff}} = \sqrt{\frac{3\pi}{32 G n_{\text{H}} \mu m_{\text{H}}}}. \quad (13)$$

We have $6.9 \times 10^3 \text{ yr} \lesssim t_{\text{ff}} \lesssim 6.5 \times 10^4 \text{ yr}$. Therefore, across the envelope, the $t_{\text{AD}}/t_{\text{ff}}$ ratio remains relatively constant to ~ 5 . This ratio is a factor of 2 lower than the expected value for low-mass proto-star (~ 10 , see e.g. Williams et al. 1998). The fact that our ratio is ~ 5 indicates that the magnetic field starts to efficiently support the envelope against gravitational collapse. In contrast, Caselli et al. (2002c) derived a value of ~ 2 for the same ratio for the L1544 pre-stellar core, indicating that it is on the verge of dynamical collapse.

Finally, based on the definition given in Nakano & Tadamaru (1972), we derive the value of the magnetic field B across the envelope:

$$B(G) = 10^{-4} \times \sqrt{\frac{8\pi\mu_0 R^2 x(\text{e}) n_{\text{H}}^2 m_{\text{H}} \langle \sigma v \rangle}{t_{\text{AD}}}}, \quad (14)$$

with μ_0 the vacuum permeability, R is the radial distance, and $\langle \sigma v \rangle \simeq 2 \times 10^{-9} \text{ cm}^3 \text{ s}^{-1}$ is the average collision rate between ions and atoms (Osterbrock 1961; Basu & Mouschovias 1994). The result is shown in the bottom panel of Fig. 9. The magnetic field varies between 6 and 46 μG , in agreement with values found in pre-stellar cores such as L1498 and L1517B (Kirk, Ward-Thompson & Crutcher 2006). This shows again that the physical properties of the envelope of IRAS16293 is close to those of cold cores, consistent with the young age of the proto-star.

7 CONCLUSIONS

¹²We have used GASS and LIME to perform a 3D modelling of HCO^+ and its isotopologues H^{13}CO^+ , HC^{18}O^+ , DCO^+ , and D^{13}CO^+ emission in the low-mass proto-star IRAS16293. We have considered an envelope, outflow, and foreground cloud structure to model the emission of these species. Thanks to the large number of detected transitions and the wide range of upper energy levels (4–389 K), we have been able to study these different structures and give good constraints on the physical conditions of the outflow and foreground cloud. The contribution of the envelope to the emission of HCO^+ clearly does not dominate, limiting the constraints we can obtain on the physical and chemical parameters. For the outflow, we have derived $T_{\text{kin}} = (200 \pm 20) \text{ K}$ and $n(\text{H}_2) = (5.5 \pm 1.5) \times 10^6 \text{ cm}^{-3}$ with $X(\text{HCO}^+) = (4 \pm 1) \times 10^{-9}$. The emission coming from the outflow is mostly responsible for all the $J_{\text{up}} \geq 8$ emission and it largely participates to other transitions. The outflow mass is $0.02 M_{\odot}$ with an outflow mass rate $\dot{M}_{\text{out}} = 6.72 \times 10^{-5} M_{\odot}$, ~ 3 times lower than the infall mass rate of the surrounding envelope. This value is in agreement with the typical ejection over accretion ratio of 0.1–0.3 found in young stellar objects. We have also demonstrated that the foreground cloud causes the deep self-absorption seen for $J_{\text{up}} \leq 4$ lines. This is only possible if this cloud is cold ($\leq 30 \text{ K}$) and not dense [$n(\text{H}_2) \leq 1 \times 10^4 \text{ cm}^{-3}$]. We have used the chemical code NAUTILUS to estimate the HCO^+ radial abundance profile of the envelope and, combined with the outflow and the foreground cloud contributions, we have been able to reproduce correctly the observed lines. By using multiple isotopologues, we also derived several fractionation ratio: $C^{13}/C = 51 \pm 5$, $^{16}\text{O}/^{18}\text{O} = 460 \pm 50$, and $\text{H}/\text{D} = 20\text{--}250$. Finally, using the HCO^+ abundance profile across the envelope, we

have been able to estimate the ionization degree to be $10^{-8.9} \lesssim x(\text{e}) \lesssim 10^{-7.9}$. The derived $x(\text{e}) - n(\text{H}_2)$ relation is consistent with the one found in pre-stellar cores. The ambipolar diffusion time-scale is ~ 5 times higher than the free-fall time-scale, indicating that the magnetic field is playing a supporting role against the gravitational collapse of the envelope. The inferred magnetic field strength is 6–46 μG , consistent with values found in pre-stellar cores.

ACKNOWLEDGEMENTS

HIFI has been designed and built by a consortium of institutes and university departments from across Europe, Canada and the United States under the leadership of SRON Netherlands Institute for Space Research, Groningen, the Netherlands, and with major contributions from Germany, France, and the USA. Consortium members are Canada: CSA, UWaterloo; France: IRAP (formerly CESR), LAB, LERMA, IRAM; Germany: KOSMA, MPIfR, MPS; Ireland: NUI Maynooth; Italy: ASI, IFSI-INAf, Osservatorio Astrofisico di Arcetri-INAf; Netherlands: SRON, TUD; Poland: CAMK, CBK; Spain: Observatorio Astronómico Nacional (IGN), Centro de Astrobiología (CSIC-INTA). Sweden: Chalmers University of Technology – MC2, RSS, and GARD; Onsala Space Observatory; Swedish National Space Board, Stockholm University – Stockholm Observatory; Switzerland: ETH Zurich, FHNW; USA: Caltech, JPL, NHSC. We thank many funding agencies for financial support. DQ acknowledges the financial support received from the STFC through an Ernest Rutherford Grant and Fellowship (proposal number ST/M004139). VW thanks the French CNRS/INSU programme PCMI and the ERC Starting Grant (3DICE, grant agreement 336474) for their funding.

REFERENCES

- Aikawa Y., Wakelam V., Garrod R. T., Herbst E., 2008, *ApJ*, 674, 984
- Arce H. G., Sargent A. I., 2005, *ApJ*, 624, 232
- Arce H. G., Sargent A. I., 2006, *ApJ*, 646, 1070
- Bachiller R., Pérez Gutiérrez M., 1997, *ApJ*, 487, L93
- Basu S., Mouschovias T. C., 1994, *ApJ*, 432, 720
- Bensch F., Pak I., Wouterloot J. G. A., Klapper G., Winnewisser G., 2001, *ApJ*, 562, L185
- Beuther H., Schilke P., Sridharan T. K., Menten K. M., Walmsley C. M., Wyrowski F., 2002, *A&A*, 383, 892
- Bottinelli S., Wakelam V., Caux E., Vastel C., Aikawa Y., Ceccarelli C., 2014, *MNRAS*, 441, 1964
- Brinch C., Hogerheijde M. R., 2010, *A&A*, 523, A25
- Caselli P., Walmsley C. M., Terzieva R., Herbst E., 1998, *ApJ*, 499, 234
- Caselli P., Walmsley C. M., Zucconi A., Tafalla M., Dore L., Myers P. C., 2002a, *ApJ*, 565, 331
- Caselli P., Walmsley C. M., Zucconi A., Tafalla M., Dore L., Myers P. C., 2002b, *ApJ*, 565, 344
- Caselli P., Benson P. J., Myers P. C., Tafalla M., 2002c, *ApJ*, 572, 238
- Castets A., Ceccarelli C., Loinard L., Caux E., Lefloch B., 2001, *A&A*, 375, 40
- Caux E. et al., 2011, *A&A*, 532, A23
- Ceccarelli C., Loinard L., Castets A., Tielens A. G. G. M., Caux E., 2000b, *A&A*, 357, L9
- Ceccarelli C. et al., 2010, *A&A*, 521, L22
- Chandler C. J., Brogan C. L., Shirley Y. L., Loinard L., 2005, *ApJ*, 632, 371
- Coutens A. et al., 2012, *A&A*, 539, A132
- Coutens A. et al., 2016, *A&A*, 590, L6
- Crimier N., Ceccarelli C., Maret S., Bottinelli S., Caux E., Kahane C., Lis D. C., Olofsson J., 2010, *A&A*, 519, A65
- Dalgarno A., Lepp S., 1984, *ApJ*, 287, L47
- Dierickx M., Jiménez-Serra I., Rivilla V. M., Zhang Q., 2015, *ApJ*, 803, 89

- Doty S. D., Schöier F. L., van Dishoeck E. F., 2004, *A&A*, 418, 1021
- Flower D. R., 1999, *MNRAS*, 305, 651
- Garrod R. T., Herbst E., 2006, *A&A*, 457, 927
- Girart J. M., Estalella R., Palau A., Torrelles J. M., Rao R., 2014, *ApJ*, 780, L11
- Gregersen E. M., Evans II N. J., Zhou S., Choi M., 1997, *ApJ*, 484, 256
- Hartquist T. W., Williams D. A., eds, 1998, *The Molecular Astrophysics of Stars and Galaxies*. Oxford Univ. Press, Oxford
- Hasegawa T. I., Herbst E., Leung C. M., 1992, *ApJS*, 82, 167
- Hily-Blant P. et al., 2010, *A&A*, 521, L52
- Hincelin U., Wakelam V., Hersant F., Guilloteau S., Loison J. C., Honvault P., Troe J., 2011, *A&A*, 530, A61
- Hogerheijde M. R., van Dishoeck E. F., Blake G. A., van Langevelde H. J., 1998, *ApJ*, 502, 315
- Hunter S. D., Digel S. W., de Geus E. J., Kanbach G., 1994, *ApJ*, 436, 216
- Jaber A. A., Ceccarelli C., Kahane C., Caux E., 2014, *ApJ*, 791, 29
- Jacobsen S. K. et al., 2018, *A&A*, 612, A72
- Jørgensen J. K., Bourke T. L., Nguyen Luong Q., Takakuwa S., 2011, *A&A*, 534, A100
- Jørgensen J. K. et al., 2016, *A&A*, 595, A117
- Kirk J. M., Ward-Thompson D., Crutcher R. M., 2006, *MNRAS*, 369, 1445
- Koumpia E., Semenov D. A., van der Tak F. F. S., Boogert A. C. A., Caux E., 2017, *A&A*, 603, A88
- Loinard L., Castets A., Ceccarelli C., Tielens A. G. G. M., Faure A., Caux E., Duvert G., 2000, *A&A*, 359, 1169
- Loinard L., Castets A., Ceccarelli C., Caux E., Tielens A. G. G. M., 2001, *ApJ*, 552, L163
- Loinard L. et al., 2013, *MNRAS*, 430, L10
- López-Sepulcre A. et al., 2015, *MNRAS*, 449, 2438
- Lucas R., Liszt H., 1996, *A&A*, 307, 237
- Majumdar L., Gratier P., Vidal T., Wakelam V., Loison J.-C., Hickson K. M., Caux E., 2016, *MNRAS*, 458, 1859
- McKee C. F., 1989, *ApJ*, 345, 782
- Mouschovias T. C., 1987, in Morfill G. E., Scholer M., eds, *Physical Processes in Interstellar Clouds*. D. Reidel Publishing Co., Dordrecht, p. 453
- Müller H. S. P., Schlöder F., Stutzki J., Winnewisser G., 2005, *J. Mol. Struct.*, 742, 215
- Mundy L. G., Wootten A., Wilking B. A., Blake G. A., Sargent A. I., 1992, *ApJ*, 385, 306
- Nakano T., Tademaru E., 1972, *ApJ*, 173, 87
- Neufeld D. A., Wolfire M. G., Schilke P., 2005, *ApJ*, 628, 260
- Ortiz-León G. N. et al., 2017, *ApJ*, 834, 141
- Osterbrock D. E., 1961, *ApJ*, 134, 270
- Ott S., 2010, in Mizumoto Y., Morita K.-I., Ohishi M., eds, *ASP Conf. Ser. Vol. 434, Astronomical Data Analysis Software and Systems XIX*. Astron. Soc. Pac., San Francisco, p.139
- Pech G., Loinard L., Chandler C. J., Rodríguez L. F., D'Alessio P., Brogan C. L., Wilner D. J., Ho P. T. P., 2010, *ApJ*, 712, 1403
- Persson M. V., Jørgensen J. K., van Dishoeck E. F., 2013, *A&A*, 549, L3
- Persson M. V., Jørgensen J. K., van Dishoeck E. F., Harsono D., 2014, *A&A*, 563, A74
- Persson M. V. et al., 2018, *A&A*, 610, A54
- Pineda J. E. et al., 2012, *A&A*, 544, L7
- Podio L., Lefloch B., Ceccarelli C., Codella C., Bachiller R., 2014, *A&A*, 565, A64
- Quénard D., Bottinelli S., Caux E., 2017a, *MNRAS*, 468, 685
- Quénard D., Vastel C., Ceccarelli C., Hily-Blant P., Lefloch B., Bachiller R., 2017b, *MNRAS*, 470, 3194
- Quénard D., Jiménez-Serra I., Viti S., Holdship J., Coutens A., 2018, *MNRAS*, 474, 2796
- Rao R., Girart J. M., Marrone D. P., Lai S.-P., Schnee S., 2009, *ApJ*, 707, 921
- Rawlings J. M. C., Taylor S. D., Williams D. A., 2000, *MNRAS*, 313, 461
- Rawlings J. M. C., Redman M. P., Keto E., Williams D. A., 2004, *MNRAS*, 351, 1054
- Richer J. S., Shepherd D. S., Cabrit S., Bachiller R., Churchwell E., 2000, in Mannings V., Boss A. P., Russell S. S., eds, *Protostars and Planets IV*. Univ. Arizona Press, Tucson, p. 867
- Roberts H., Millar T. J., 2000, *A&A*, 361, 388
- Roelfsema P. R. et al., 2012, *A&A*, 537, A17
- Rollins R. P., Rawlings J. M. C., Williams D. A., Redman M. P., 2014, *MNRAS*, 443, 3033
- Ruud M., Wakelam V., Hersant F., 2016, *MNRAS*, 459, 3756
- Sánchez-Monge Á., López-Sepulcre A., Cesaroni R., Walmsley C. M., Codella C., Beltrán M. T., Pestalozzi M., Molinari S., 2013, *A&A*, 557, A94
- Savage C., Ziurys L. M., 2004, *ApJ*, 616, 966
- Schöier F. L., Jørgensen J. K., van Dishoeck E. F., Blake G. A., 2002, *A&A*, 390, 1001
- Schöier F. L., van der Tak F. F. S., van Dishoeck E. F., Black J. H., 2005, *A&A*, 432, 369
- Shu F. H., 1977, *ApJ*, 214, 488
- Shu F. H., Adams F. C., Lizano S., 1987, *ARA&A*, 25, 23
- Shu F. H., Lizano S., Ruden S. P., Najita J., 1988, *ApJ*, 328, L19
- Smith R. L., Pontoppidan K. M., Young E. D., Morris M. R., 2015, *ApJ*, 813, 120
- Spitzer L., 1978, *Physical Processes in the Interstellar Medium*. Wiley-Interscience, New York
- Stark R. et al., 2004, *ApJ*, 608, 341
- Tafalla M., Santiago-García J., Hacar A., Bachiller R., 2010, *A&A*, 522, A91
- van Dishoeck E. F., Blake G. A., Jansen D. J., Groesbeck T. D., 1995, *ApJ*, 447, 760
- Vastel C. et al., 2010, *A&A*, 521, L31
- Visser R. et al., 2012, *A&A*, 537, A55
- Wakelam V., Vastel C., Aikawa Y., Coutens A., Bottinelli S., Caux E., 2014, *MNRAS*, 445, 2854
- Wakelam V. et al., 2015, *ApJS*, 217, 20
- Williams J. P., Bergin E. A., Caselli P., Myers P. C., Plume R., 1998, *ApJ*, 503, 689
- Wilson T. L., Rood R., 1994, *ARA&A*, 32, 191
- Wootten A., 1989, *ApJ*, 337, 858
- Yeh S. C., Hirano N., Bourke T. L., Ho P. T., Lee C.-F., Ohishi N., Takakuwa S., 2008, *ApJ*, 675, 454
- Zhang Q., Hunter T. R., Brand J., Sridharan T. K., Cesaroni R., Molinari S., Wang J., Kramer M., 2005, *ApJ*, 625, 864

APPENDIX: LINE PROFILES

In this appendix, we present the line profiles of HCO^+ , H^{13}CO^+ , HC^{18}O^+ , DCO^+ , and D^{13}CO^+ observed transitions compared to the best-fitting model. Please note that the observed HC^{18}O^+ transition at 255.5 GHz is badly calibrated, as suggested by Caux et al. (2011), explaining the large difference between the observation and the model. Differences between the model and the observation line profiles for low- J transitions ($\lesssim 350$ GHz) may be due to inhomogeneities in the envelope structure (see Section 6.1).

The HCO^+ (3–2) and (4–3) lines, observed at APEX, are clearly much brighter than the other lines, and their intensities cannot be reproduced by our model that reproduces well all other lines. We suspect an intensity calibration problem for these two lines, for which we nevertheless correctly reproduce the line profiles.

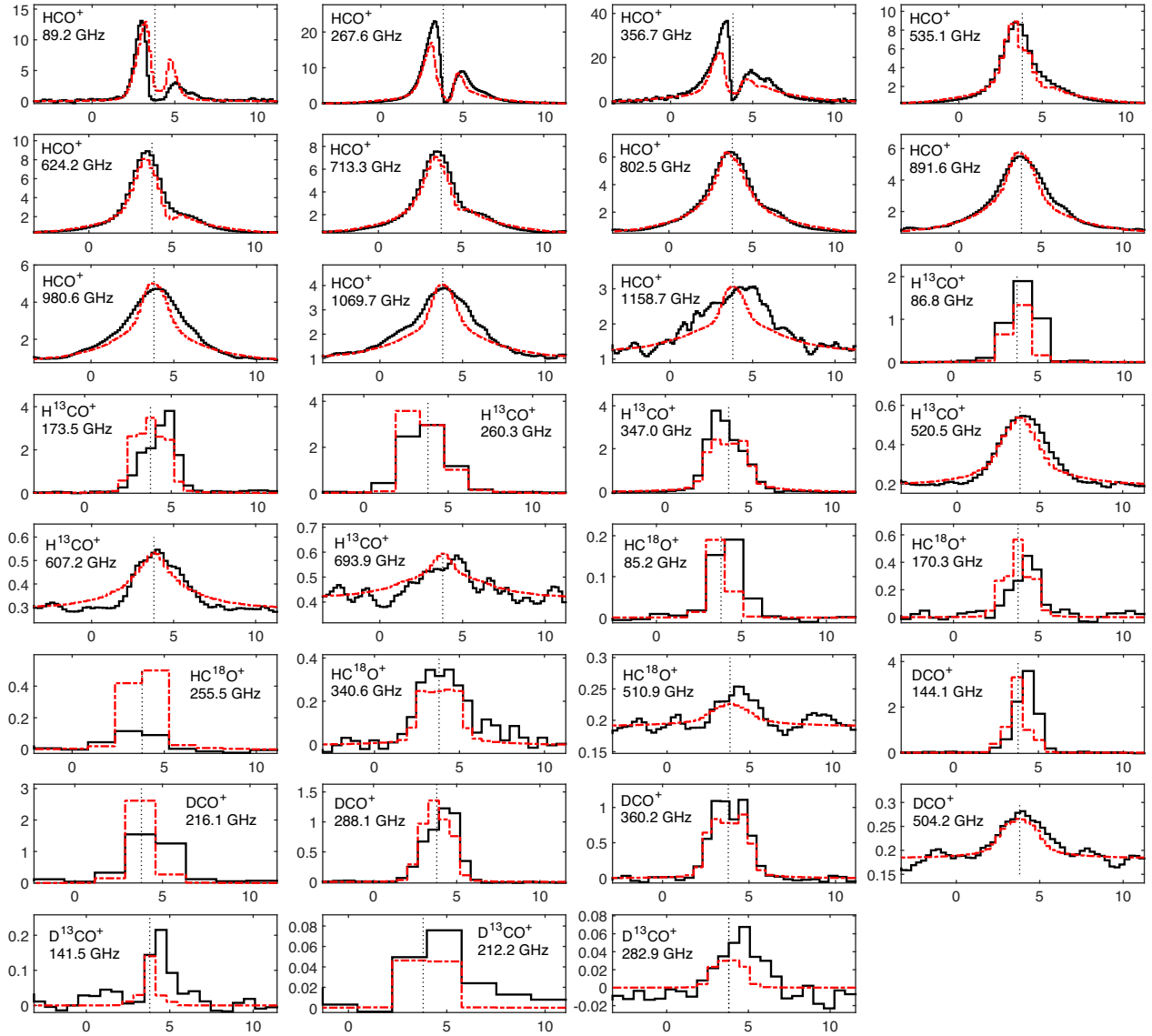


Figure A1. Main beam temperature (in K) of HCO^+ , H^{13}CO^+ , HC^{18}O^+ , DCO^+ , and D^{13}CO^+ observed transitions (in black) compared to the best-fitting model (in red) as a function of the velocity (in km s^{-1}). The vertical black dotted line shows the $V_{\text{LSR}} = 3.8 \text{ km s}^{-1}$ of IRAS16293. Note that the observed HC^{18}O^+ transition at 255.5 GHz is badly calibrated, as suggested by Caux et al. (2011).

This paper has been typeset from a \LaTeX file prepared by the author.